IEEE Access
Multidisciplinary | Rapid Review | Open Access Journal

Received October 2, 2019, accepted October 28, 2019, date of publication November 4, 2019, date of current version December 12, 2019.

Digital Object Identifier 10.1109/ACCESS.2019.2951361

Cost-Effective Predictive Flux Control for a Sensorless Doubly Fed Induction Generator

MAHMOUD A. MOSSA[1], AMEENA SAAD AL-SUMAITI[2], (Member, IEEE), TON DUC DO[3], (Senior Member, IEEE), AND AHMED A. ZAKI DIAB[1]

[1]Electrical Engineering Department, Faculty of Engineering, Minia University, Minya 61111, Egypt
[2]Advanced Power and Energy Center, Department of Electrical and Computer Engineering, Khalifa University, Abu Dhabi, United Arab Emirates
[3]Department of Robotic Engineering, School of Engineering and Digital Sciences (SEDS), Nazarbayev University, Z05H0P9 Nur-Sultan, Kazakhstan

Corresponding authors: Mahmoud A. Mossa (mahmoud_a_mossa@mu.edu.eg) and Ton Duc Do (doduc.ton@nu.edu.kz)

This work was supported in part by Khalifa University, Abu Dhabi, United Arab Emirates under Award FSU-2018-25, and in part by the Nazarbayev University, Kazakhstan, under the NU-ORAU Program, under Award SST2017030.

ABSTRACT The paper introduces a cost effective predictive flux control (PFC) approach for a sensorless doubly fed induction generator (DFIG). The base operation of the proposed PFC depends on controlling the rotor flux (α-β) components using a cost function which is derived through analyzing the relationship between the developed torque and the angular slip frequency. To improve the rotor flux estimation and prediction, an effective rotor flux observer is proposed. A robust rotor position estimator is proposed to guarantee a precise co-ordinate transformation. In order to save the cost, only one rotor current sensor is utilized to evaluate the rotor currents. The finite control set (FCS) principle is utilized to select the voltage vectors which enables the elimination of the pulse width modulation (PWM). To validate the feasibility of the proposed sensorless PFC approach, a comprehensive comparison is carried out between the proposed sensorless PFC and the predictive torque control (PTC) for the DFIG. The obtained results confirm and emphasize the superiority of the proposed PFC in achieving the control objectives with lower ripples content and less computational burdens. Moreover, the effectiveness of the rotor position and rotor flux estimators has been confirmed through the obtained results.

INDEX TERMS Doubly fed induction generator (DFIG), predictive control, flux control, torque control, sensorless, flux estimation, current estimation, finite control set (FCS).

I. INTRODUCTION

Improving the dynamic performance of the doubly fed induction generator (DFIG) has been paid great attention [1]–[5]. This is due to the various merits which the DFIG possesses in comparison with other generation units used by the wind energy systems. For example, compared with fixed speed generators such as synchronous generators, the DFIG has the ability to work at different operating wind speeds with high capability of wind power extraction whatever the value of wind speed is. Moreover, due to the physical construction of the DFIG, its control can be realized through both stator and rotor terminals [6]–[8]. Controlling the DFIG from its rotor terminals has enabled using low power rating converters which can operate at fractions of the DFIG rated power; which saves the cost of the converters to be used. Moreover, the DFIG exhibits high capability in riding through the grid faults through adopting the appropriate fault ride-through methodology which can be applied through the rotor terminals [9]–[11].

The direct power control (DPC) principle of the DFIG has been extensively investigated through various research studies [12]–[17]. The DPC operation principle has based upon controlling the generated active and reactive powers of the DFIG through regulating the direct and quadrature axis components of the rotor current. The DPC is considered as a transformation of the direct torque control (DTC) principle which has been implemented to the induction motor drives earlier. In DPC, controlling the active power results in controlling the developed torque due to the inherent coupling between the active power and the developed torque; while controlling the reactive power results in controlling the flux level inside the machine. Based on this hypothesis, the DPC approach has been firstly applied using the same configuration of the classic DTC which utilized two hysteresis power comparators (active and reactive comparators) to provide the

The associate editor coordinating the review of this manuscript and approving it for publication was Zhuang Xu.

logic states to a look-up table in order to select the appropriate voltage vectors to be applied to the rotor terminals [13]–[17]. The classic DPC approach has managed in achieving the control objectives, but on the other hand it has suffered from noticeable ripples in the controlled variables and this was due to the fact that the selected rotor voltage vector from the look-up table has been applied for the entire control cycle to reduce the active or reactive power error, and during this it may happened that the error of one controlled variable start to decrease while the applied voltage vector continues to make negative variation of the error which means that the error will increase in the other direction and thus the ripple (deviation) is increased again.

As an attempt to avoid the shortages in the classic DPC, the predictive control (PC) technique has been utilized [18]–[21]. In this approach the hysteresis comparators are replaced with a cost effective function which minimizes the error between the reference and predicted values of the active and reactive powers, and the voltage vectors selection has been carried out based on the minimization of this cost function through two procedures; one of them has used the finite control set (FCS) principle to select the optimal voltage vector from a specified number of vectors (0....7) without using any pulse width modulation (PWM) strategy [17], [18], while the other has depended on utilizing a certain PWM procedure for voltage selection purpose [20], [21]. The former one (FCS-PC) introduces simpler configuration compared with the PWM based PC approach and this has motivated the majority of the researchers to adopt it in their studies.

The predictive control (PC) principle has been adopted with the torque and power control as well for the DFIG [22]–[24]. Although the hysteresis comparators and look-up tables were eliminated and the control configuration become simpler, but both the predictive torque control (PTC) and predictive power control (PPC) were suffering from the remarkable ripples content in the controlled variables. The reason for that can be inferred to the previous mentioned explanation which states that the selected voltage vector is applied for the entire sampling interval without any updating within the sampling interval. Another reason for that may be due to the selected value of the weighting factor used by the cost function which needs to be precisely selected as it weights the controlled variables respecting to each other's. The weighting factor plays a vital role in balancing the importance and priority of the control for the variables whatever being the torque and rotor flux in case of predictive torque control (PTC) or the active and reactive powers as in the predictive power control (PPC).

Various attempts have been made to derive an optimal value for the weighting factor through adopting an online optimization technique which updates the weighting factor according to the instantaneous change of the controlled variables respecting to their references [25], [26]. The disadvantage of this technique is that it adds extra computation burdens on the controller which cannot be realized by all microprocessors.

Recent studies have contributed to the state of the art of predictive torque control (PTC) of DFIG under unbalanced grid voltage as introduced in [27]. In this study, an efficient predictive direct torque schem has been implemented to limit the torque and power pulsations under stady state and transient conditions. In [28], a direct power control (DPC) technique has been proposed to enhance the performance of the DFIG under unbalanced condition through using of four-switch three-phase converter.

As an attempt to investigate more about the optimal control configuration for the DFIG through which various control objectives can be achieved; avoiding the shortages in previous methods and adding new contributions to the literature; the current paper introduces an effective predictive flux control (PFC) procedure which can be used with the DFIG as an effective alternate to the predictive torque and power control approaches. The operation principle of the proposed PFC is based on controlling the alpha-beta (α-β) components of the rotor flux using a simple cost function. The cost function is consisting of two terms of similar nature (only flux) and thus there is no need to use a weighting factor as in classic PTC or PPC. All of this contributed in simplifying the control structure, saving the computation time and reducing the switching losses as well. The rotor flux reference (α-β) components are obtained via analyzing the relationship between the developed electromagnetic torque and the angular slip frequency. In order to improve the estimation and prediction of the rotor flux components, an effective rotor flux estimator has been proposed. The proposed flux estimator is then used to estimate the rotor position which is used for the co-ordinates transformation needed to implement the control system. To reduce the overall cost, only one rotor current sensor is utilized while a current estimator is proposed to calculate the second phase rotor current.

It is worth to mention that the proposed PFC is utilizing a simpler cost function form compared with that ones which have been used by the PTC and PPC procedures. The cost function of the proposed PFC is consisting of two terms with the same nature (rotor flux α-β components) which enables the elimination of the weighting factor used by the classic predictive techniques. Moreover, dealing with two terms of same nature is effectively helping in reducing the computational burdens and switching losses as well and this is confirmed through the obtained results.

To validate the effectiveness of the proposed PFC and illustrate its superiority over the PTC approach, extensive tests have been carried out with the help of Fast Fourier Transform (FFT) analysis. The obtained results show that the performance of the DFIG under the proposed PFC is effectively enhanced through reducing the ripple contents in the controlled variables and through reducing the computational time and saving the energy. Moreover, the validity of the rotor current estimation is verified which confirm the effectiveness of the current estimator in replacing the sensor and saving the cost. In addition, the effectiveness and robustness of the proposed rotor position estimator is verified through the

precise estimation of the position in wide speed variations under a mismatch in the stator resistance.

The contributions of the current study can be summerized as follows

i. The proposed PFC has not been introduced and used before with the DFIG. In addition, it can be extended to be applied for different types of AC machine drives.
ii. The design and construction of the proposed PFC have been carried out in a systematic and detailed manner so that the researchers can investigate more about the base principle of the proposed PFC.
iii. The paper has introduced a robust rotor flux and rotor position observer with a detailed analysis for the observer's response under different operating frequencies through utilizing the Bode plot diagrams and through analyzing the system transfer functions.
iv. A simple and effective method for limiting the number of rotor current sensors is introduced, so that only one rotor current sensor can be utilized which reduces the cost of the overall system configuration.
v. A procedure for determining the commutation losses has been introduced, which can be used with different types of AC machine drives.
vi. A detailed comparison in terms of total harmonics distortion (THD), average absolute error (as an indication of the ripples content in the controlled variables), number of commutations, switching frequencies, switching power losses and computational time under various operating conditions of DFIG has been carried out for the proposed PFC and PTC approaches as well. Moreover, a detailed view of the action taken by the two control approaches has been presented, which clarify the control response at each instant happened that the controlled variables deviate from their references.

The paper is organized as follows: in section II, the mathematical model of DFIG is introduced in detail. Section III introduces the predictive torque control (PTC) for DFIG. Section IV presents the proposed predictive flux control (PFC). Section V presents the cost-effective rotor current estimation procedure. Furthermore, the proposed rotor flux and rotor position estimator is introduced in section VI. The test results and analysis are presented in section VII. moreover, the conclusion is stated in section VIII.

II. MATHEMATICAL MODEL OF DFIG

To implement the proposed PFC approach, a discretized time model for the DFIG is utilized. The mathematical model of the DFIG is defined in a synchronous reference frame which is rotating with the angular speed $\omega_{\bar{\psi}_s}$ of the stator flux vector $\bar{\psi}_s$. The equivalent circuit is shown in Figure 1 in which the superscript $^{'sf'}$ refers to the stator flux frame in which the stator flux is aligned to the d-axis of the synchronous rotating frame [7], [12] and [13].

The parameters R_s and R_r refer to the stator and rotor resistances, while the parameters L_{ls}, L_{lr} and L_m denote to

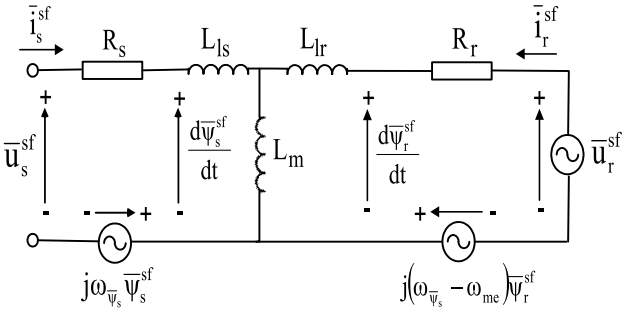

FIGURE 1. Equivalent circuit of DFIG in synchronous reference frame.

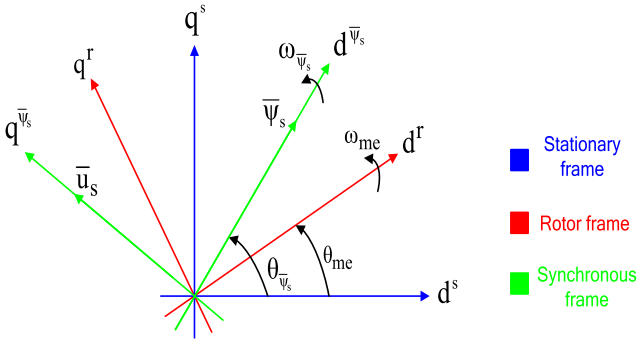

FIGURE 2. Space vectors orientation in different frames.

the leakage stator and rotor inductances and magnetizing inductance, respectively. The variables $\bar{u}_s^{sf}$ and $\bar{i}_s^{sf}$ refer to the stator voltage and current vectors defined in the synchronous rotating frame, while the variables $\bar{u}_r^{sf}$ and $\bar{i}_r^{sf}$ refer to the rotor voltage and current vectors. The variables $\bar{\psi}_s^{sf}$ and $\bar{\psi}_r^{sf}$ refer to the stator and rotor fluxes and $\omega_{\bar{\psi}_s}$, ω_{me} refer to the synchronous and mechanical angular frequencies, respectively.

From Figure 1, the dynamics of the DFIG can be outlined using the following relationships defined in a discrete form at instant kT_s, where T_s is the sampling time.

$$\bar{u}_{s,k}^{sf} = R_s \bar{i}_{s,k}^{sf} + \frac{d\bar{\psi}_{s,k}^{sf}}{dt} + j\omega_{\bar{\psi}_{s,k}} \bar{\psi}_{s,k}^{sf} \quad (1)$$

$$\bar{u}_{r,k}^{sf} = R_r \bar{i}_{r,k}^{sf} + \frac{d\bar{\psi}_{r,k}^{sf}}{dt} + j\left(\omega_{\bar{\psi}_{s,k}} - \omega_{me,k}\right) \bar{\psi}_{r,k}^{sf} \quad (2)$$

The space vector allocation for the variables in different reference frames can be shown through Figure 2, in which it can be noticed that the stator flux vector $\bar{\psi}_s^{sf}$ is aligned with the $d^{\bar{\psi}_s}$-axis of the rotating synchronous frame which rotates with an angular frequency of $\omega_{\bar{\psi}_s}$.

From Figure 2, it can be also realized that the stator flux vector makes an angle of $\theta_{\bar{\psi}_s}$ with the d^s-axis of the stationary frame, while the rotor frame rotates with an angular frequency of ω_{me} and makes an angle of θ_{me} with d^s-axis of the stationary frame. It can be realized also that the stator voltage vector $\bar{u}_s$ is leading the stator flux vector by an angle 90° and thus it is aligned to the $q^{\bar{\psi}_s}$-axis of the rotating synchronous frame. The superscripts $^{'s'}$ and $^{'r'}$ refer to the stator and rotor reference frames, respectively.

Under steady state operation of the DFIG, and under the stator field orientation (SFO) described previously, the following relationships are obtained in discrete forms as

$$\psi_{ds,k}^{sf} = \left|\bar{\psi}_{s,k}^{sf}\right|, \quad \text{and } \psi_{qs,k}^{sf} \cong 0.0 \tag{3}$$

$$u_{ds,k}^{sf} \cong 0.0, \quad \text{and } u_{qs,k}^{sf} = \left|\bar{u}_{s,k}^{sf}\right| \tag{4}$$

Based on (3) and (4), the electromagnetic torque can be calculated by

$$T_{e,k} = 1.5p\psi_{ds,k}^{sf} i_{qs,k}^{sf} \tag{5}$$

where p refers to the pole pairs. Moreover, the generated active and reactive power under the SFO can be also calculated by

$$P_{s,k} = 1.5u_{qs,k}^{sf} i_{qs,k}^{sf}, \quad \text{and } Q_{s,k} = 1.5u_{qs,k}^{sf} i_{ds,k}^{sf} \tag{6}$$

The active and reactive powers can be also expressed in terms of the rotor current *d-q* components after utilizing the flux-current relationships as follows

$$P_{s,k} = -1.5\frac{L_m}{L_s} u_{qs,k}^{sf} i_{qr,k}^{sf}, \quad \text{and}$$

$$Q_{s,k} = 1.5\frac{L_m}{L_s} u_{qs,k}^{sf} \left(\frac{u_{qs,k}^{sf}}{L_m \omega_{\bar{\psi}_{s,k}}} - i_{dr,k}^{sf}\right) \tag{7}$$

The relationships in (6) and (7) will be utilized later to derive the references of the d-q components of the stator and rotor currents and then the reference value of the rotor flux needed to apply the predictive torque control can be obtained.

III. PREDICTIVE TORQUE CONTROL (PTC) FOR DFIG

The operation of the predictive torque control is relied on controlling the developed torque and rotor flux of the DFIG [29]. The core of the PTC depends on the used cost function which is consisting of two terms; the first which is the torque error (error between the reference torque $T_{e,k+1}^{*}$ and predicted torque $\tilde{T}_{e,k+1}$ value at instant $(k+1)T_s$), while the second term is the rotor flux error (error between the rotor flux reference $\bar{\psi}_{r,k+1}^{*}$ and predicted rotor flux $\tilde{\psi}_{r,k+1}$ at instant $(k+1)T_s$) and this can be expressed in a cost function form by

$$C_{k+1}^{i} = \left|T_{e,k+1}^{*} - \tilde{T}_{e,k+1}\right|^{i} + w_f \left|\bar{\psi}_{r,k+1}^{*} - \tilde{\psi}_{r,k+1}\right|^{i} \tag{8}$$

where ^{i} refers to the voltage index (0.....7), while the superscript $\tilde{}$ refers to the predicted value.

It can be realized that the cost function of (8) for the PTC procedure is using a weighting factor w_f to balance the weighting of the rotor flux error respecting to the torque error. The determination of w_f is a sensitive issue which can lead to deteriorating the weighting balance between the torque variation and rotor flux variation if it is not selected properly. However, an online tuning of w_f can contribute in restricting the ripple contents in the controlled variables, but it adds extra computational burdens to the controller which in sequence increases the switching losses. For this reason, the proposed

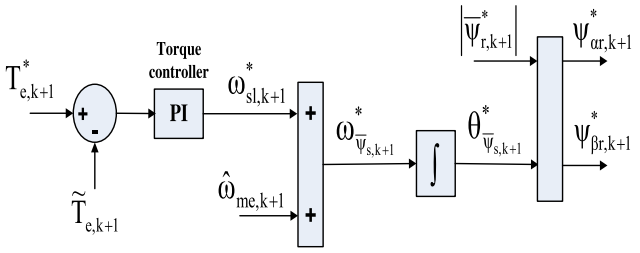

FIGURE 3. Operation methodology of the PI torque controller.

PFC approach is utilized a weighting factor free cost function as will be illustrated in the following section.

The reference of the rotor flux $\psi_{r,k+1}^{*}$ is calculated using the reference *d-q* components of stator and rotor currents calculated from (6) and (7) in terms of reference active and reactive powers as follows

$$i_{qs,k}^{*} = \frac{P_{s,k}^{*}}{1.5u_{qs,k}^{sf}}, \quad \text{and } i_{ds,k}^{*} = \frac{Q_{s,k}^{*}}{1.5u_{qs,k}^{sf}} \tag{9}$$

$$i_{qr,k}^{*} = \frac{P_{s,k}^{*}}{-1.5\frac{L_m}{L_s}u_{qs,k}^{sf}}, \quad \text{and } i_{dr,k}^{*} = \frac{u_{qs,k}^{sf}}{L_m \omega_{\bar{\psi}_{s,k}}} - \frac{Q_{s,k}^{*}}{1.5\frac{L_m}{L_s}u_{qs,k}^{sf}} \tag{10}$$

Then, the reference *d-q* components of rotor flux can be calculated by

$$\psi_{dr,k}^{*} = L_r i_{dr,k}^{*} + L_m i_{ds,k}^{*}, \quad \text{and } \psi_{qr,k}^{*} = L_r i_{qr,k}^{*} + L_m i_{qs,k}^{*} \tag{11}$$

From (11), the modulus of rotor flux reference to be used in (8) is calculated at instant $(k+1)T_s$ by

$$\left|\bar{\psi}_{r,k+1}^{*}\right| = \sqrt{\left(\psi_{dr,k}^{*}\right)^2 + \left(\psi_{qr,k}^{*}\right)^2} \tag{12}$$

While, the reference torque $T_{e,k+1}^{*}$ can be also calculated at instant $(k+1)T_s$ under SFO by

$$T_{e,k+1}^{*} = 1.5p\left(\frac{u_{qs,k+1}^{sf} i_{qs,k+1}^{*} - R_s\left(i_{qs,k+1}^{*}\right)^2}{\omega_{\bar{\psi}_{s,k+1}}}\right) \tag{13}$$

The predicted value of the torque $\tilde{T}_{e,k+1}$ can be calculated started from (5) and (1), while the predicted value of the rotor flux $\tilde{\psi}_{r,k+1}$ can be evaluated with the help of (2).

Till now, all terms required by the cost function (8) are acquirable and then (8) can be utilized by the PTC approach.

IV. PROPOSED PREDICTIVE FLUX CONTROL (PFC)

The operation principle of the proposed PFC is based on deriving a cost function form which consists of the errors between the references and predicted values of the rotor flux components ($\tilde{\psi}_{\alpha r,k+1}$ and $\tilde{\psi}_{\beta r,k+1}$). The predicted values of the rotor flux components can be easily obtained with the help of (2) when defined in the stationary reference frame, while the core idea is standing behind the derivation of the references of the rotor flux components ($\psi_{\alpha r,k+1}^{*}$ and $\psi_{\beta r,k+1}^{*}$)

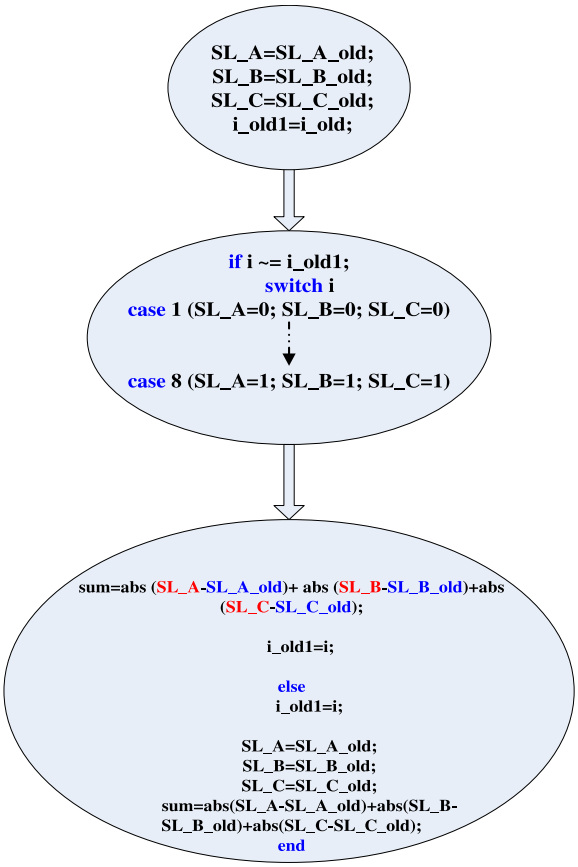

FIGURE 4. Calculation the number of commutations.

which is analyzed and described in a systematic manner as following.

The rotor flux reference components $\psi^*_{\alpha r,k+1}$ and $\psi^*_{\beta r,k+1}$ are derived through analyzing the relationship between the electromagnetic torque $\tilde{T}_{e,k+1}$ and the angular slip frequency $\omega_{sl,k+1}$ between the stator flux vector and rotor flux vector.

Via utilizing the relationships of (1) and (2) and after some mathematical derivations, the rotor flux variation (derivative) can be expressed in terms of the stator flux variation at instant $(k+1)T_s$ as follows

$$\frac{d\bar{\psi}^{sf}_{r,k+1}}{dt} = \frac{L_r L_t}{(R_r L_m - L_r L_t)}\left[\frac{R_r}{L_t}\frac{d\bar{\psi}^{sf}_{s,k+1}}{dt} - \bar{u}^{sf}_{r,k+1} + j\left(\omega_{\bar{\psi}_{s,k+1}} - \omega_{me,k+1}\right)\bar{\psi}^{sf}_{r,k+1}\right] \quad (14)$$

Then, by taking the Laplace transform of (14), it results

$$\bar{\psi}^{sf}_{r,k+1}(S) = \frac{L_r R_r S\bar{\psi}^{sf}_{s,k+1}(S) - L_r L_t \bar{u}^{sf}_{r,k+1}(S)}{\left((R_r L_m - L_r L_t)S - jL_r L_t\left(\omega_{\bar{\psi}_{s,k+1}} - \omega_{me,k+1}\right)\right)} \quad (15)$$

where $L_t = L_s - \frac{L_m^2}{L_r}$ refers to the stator transient inductance.

From (15), it can be realized that the rotor flux has a time constant of $T_f = (R_r L_m - L_r L_t)$ by which it adapts its change with respect to the applied rotor voltage $\bar{u}^{sf}_{r,k+1}$ and the specified stator flux $\bar{\psi}^{sf}_{s,k+1}$ which is supposed to be with constant value under normal grid conditions.

The stator flux magnitude can be determined under the SFO by

$$\left|\bar{\psi}_{s,k+1}\right| = \psi^{sf}_{qs,k+1} = \left|\frac{\bar{u}^{sf}_{s,k+1}}{\omega_{\bar{\psi}_{s,k+1}}}\right| = 1.20Vs \quad (16)$$

The stator and rotor flux vectors can be also expressed in exponential forms at instant $(k+1)T_s$ by

$$\bar{\psi}_{s,k+1} = \left|\bar{\psi}_{s,k+1}\right| e^{j\omega_{\bar{\psi}_{s,k+1}}t}, \quad \text{and } \bar{\psi}_{r,k+1} = \left|\bar{\psi}_{r,k+1}\right| e^{j\omega_{me,k+1}t} \quad (17)$$

Via utilizing (17), the electromagnetic torque of the DFIG can be calculated by

$$T_{e,k+1} = 1.5p\frac{L_m}{L_t L_r}\left|\bar{\psi}_{s,k+1}\right| e^{j\omega_{\bar{\psi}_{s,k+1}}t} \times \left|\bar{\psi}^*_{r,k+1}\right| e^{j\omega_{\bar{\psi}_{me,k+1}}t} \quad (18)$$

where $\times$ denotes to the cross product. Then, from (16) and (18), the torque can be expressed by

$$T_{e,k+1} = 1.20 * 1.5p\frac{L_m T_f}{L_t L_r}\left|\bar{\psi}^*_{r,k+1}\right|\left(1 - e^{\frac{-t}{T_f}}\right) * \left(\frac{\overbrace{\omega_{Sl,k+1}}}{\omega\bar{\psi}_{S,k+1} - \omega_{me,k+1}}\right) \quad (19)$$

where $\left|\bar{\psi}^*_{r,k+1}\right|$ is calculated by (12) as stated earlier and which is supposed to give a constant value almost equals 1.223 Vs.

From (19), it can be realized that under normal grid conditions and with fixed stator flux magnitude, the torque can be managed through regulating the angular slip frequency $\omega_{sl,k+1} = \omega_{\bar{\psi}_{s,k+1}} - \omega_{me,k+1}$ when the rotor flux reference $\bar{\psi}^*_{r,k+1}$ is kept constant.

Thus, for a given torque reference $T^*_{e,k+1}$, there will be a correspondent reference value of $\omega^*_{sl,k+1}$. The values of $\omega^*_{sl,k+1}$ are utilized to obtain the references of the angular synchronous frequency $\omega^*_{\bar{\psi}_{s,k+1}}$ which are then used to calculate the rotor flux reference values ($\psi^*_{\alpha r,k+1}$ and $\psi^*_{\beta r,k+1}$) which are utilized by the cost function of the proposed PFC. The design procedure of the PI torque controller which will be used to obtain $\omega^*_{sl,k+1}$ is performed as follows

From (19), the term $K = 1.20 * 1.5p\frac{L_m T_f}{L_t L_r}\left|\bar{\psi}^*_{r,k+1}\right|$ is considered as a constant, and then by differentiating (19) respecting to the time, this results in

$$\frac{dT_{e,k+1}}{dt} = K * \omega_{sl,k+1} * \frac{1}{T_f}e^{\frac{-t}{T_f}} \quad (20)$$

By taking the Laplace transform of (20), this results in

$$ST_{e,k+1}(S) = \frac{K}{T_f} * \frac{1}{\left(S + \frac{1}{T_f}\right)}\omega_{sl,k+1}(S) \quad (21)$$

Moreover, the dynamic behavior of the PI torque controller can be described by

$$\omega^*_{sl,k+1}(S) = \left(k_p + \frac{k_i}{S}\right) * \left(T^*_{e,k+1}(S) - T_{e,k+1}(S)\right) \quad (22)$$

From (21), the transfer function which describes the relationship between $\omega_{sl,k+1}$ as an output and $T_{e,k+1}$ as an input can be expressed by

$$\frac{\omega_{sl,k+1}(S)}{T_{e,k+1}(S)} = \frac{ST_f}{K}\left(S + \frac{1}{T_f}\right) \quad (23)$$

By substituting from (23) into (22), it results

$$T_{e,k+1}(S) * \frac{ST_f}{K}\left(S + \frac{1}{T_f}\right) = \left(k_p + \frac{k_i}{S}\right) * \left(T^*_{e,k+1}(S) - T_{e,k+1}(S)\right) \quad (24)$$

By dividing both sides by $T^*_{e,k+1}(S)$, and after abbreviations, this results in

$$\frac{T_{e,k+1}(S)}{T^*_{e,k+1}(S)} = \frac{k_p S + k_i}{\frac{T_f}{K}S^3 + \frac{1}{K}S^2 + k_p S + k_i} \quad (25)$$

In order to obtain stable dynamic response from the PI torque controller, the characteristic equation which outlines its operation must be with real negative roots to have smooth damping for the signal oscillation until it reaches to its steady state value.

The denominator of (25) represents the characteristic equation of the PI torque controller, thus via analyzing equation, the roots which achieve stable response can be obtained as follows

$$S^3 + \frac{1}{T_f}S^2 + K\frac{k_p}{T_f}S + \frac{k}{T_f}k_i = 0.0 \quad (26)$$

On the other hand, the open-loop (*ol*) dynamics for a third order system can be described by the following expression

$$H_{ol}(S) = \frac{G(S+z)}{S^2(S+P)} \quad (27)$$

where z and P represent the zero and pole of the open-loop dynamic response of the system, and G is the open-loop gain. The z and P have a direct relationship with the natural frequency ω_n and damping factor ζ of the system and which can be expressed by

$$\zeta = \sqrt{\frac{G}{4z}}, \quad \text{and } G = \omega_n, \quad \text{and } P = 2\zeta\omega_n \quad (28)$$

In the same manner, the closed-loop (*cl*) dynamics of a third order system can be represented by the following transfer function

$$H_{cl}(S) = \frac{H_{ol}(S)}{1 + H_{ol}(S)} = \frac{G(S+z)}{S^3 + PS^2 + GS + Gz} \quad (29)$$

The denominator of (29) gives the characteristic equation which identifies the desired closed-loop dynamics in terms of natural frequency ω_n and damping factor ζ for a third order system which can be represented by

$$S^3 + 2\zeta\omega_n S^2 + \omega_n S + \frac{\omega_n^2}{4\zeta^2} = 0.0 \quad (30)$$

Now, by comparing the (26) and (30), the coefficients k_p and k_i of the PI torque controller can be calculated by

$$k_p = \frac{T_f}{K}\omega_n, \quad \text{and } k_i = \frac{T_f\omega_n^2}{4K\zeta^2} \quad (31)$$

After designing the PI torque controller, the reference angular slip frequency $\omega^*_{sl,k+1}$ can be obtained and then it is added to the estimated mechanical speed $\hat{\omega}_{me,k+1}$ to get the reference angular synchronous frequency $\omega^*_{\bar{\psi}_{s,k+1}}$ which is integrated to get $\theta^*_{\bar{\psi}_{s,k+1}}$ which is then used besides $\left|\bar{\psi}^*_{r,k+1}\right|$ to get the reference rotor flux α-β components as shown in Figure 3.

Now, the cost function to be used by the proposed PFC approach can be formulated by

$$\wedge^i_{k+1} = \left|\psi^*_{\alpha r,k+1} - \tilde{\psi}_{\alpha r,k+1}\right|^i + \left|\psi^*_{\beta r,k+1} - \tilde{\psi}_{\beta r,k+1}\right|^i \quad (32)$$

Compared with (8), the cost function form of (32) is simpler and does not require using a weighting factor value. Moreover, it can be expected that (32) will exhibit less computational time than (8), and this can be referred to that (8) contains the torque and rotor flux errors, the torque itself needs to be estimated using other variables which increases the computational time per each control cycle.

The number of commutations which can be considered as an indication to the computation burden on the controller can be calculated using only the voltage index $'i'$ as an input variable. This fact is realized through analyzing the behavior of the inverter switches in each of the three legs (*A,B,C*) at each time happened that the voltage index changes its sector. When the voltage index changes its value, the inverter switches update their states (on/off). The variation of the states can be transformed into binary logic forms (0 or 1), and then if the binary logic difference between the present logic state of the switch and its previous one is stored and by summing all logic differences, the total number of commutations can be obtained. Figure 4 shows the code sequence for computing the commutations number in which the voltage index (i) is the input and number of commutations is identified as the output.

Through comparing the formulations of the proposed PFC which utilizes the cost function of (32) and the PTC which implements the cost function of (8), it can be expected that the time taken by the PTC cost function will be larger than the time taken by the PFC cost function. This can be easily realized through analyzing the cost functions terms, for example in (8), the calculations are performed for the rotor flux and torque; the latter involves within it the calculation of the rotor flux again. Moreover, the calculation of the weighting factor adds extra. On the other hand, the terms used in (32) are only of the rotor flux components which do not need long

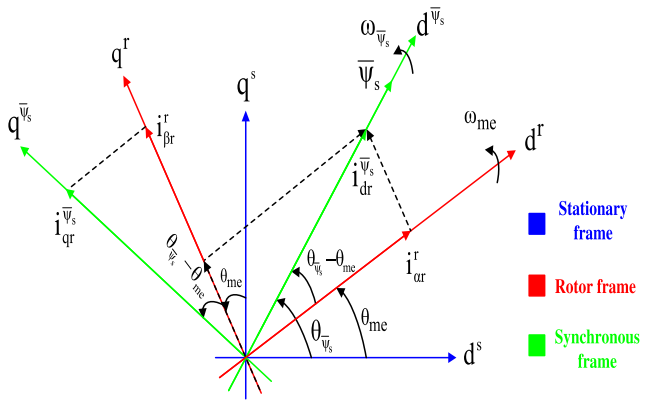

FIGURE 5. Space vector representation of rotor currents in three different reference frames.

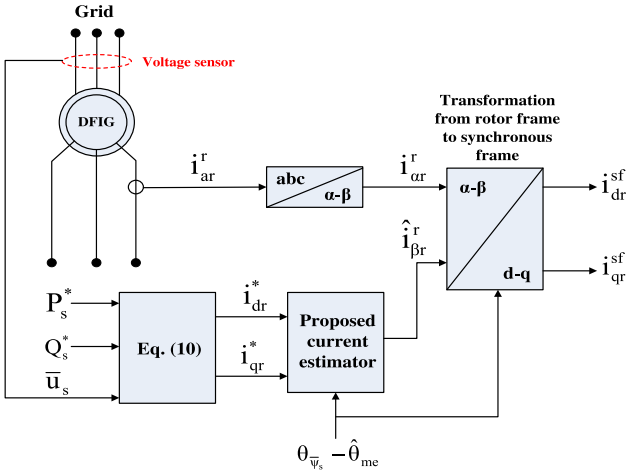

FIGURE 6. Rotor current estimation.

time to be calculated; moreover, there is no need for using a weighting factor in this case.

The next important step is to enhance the estimation of the rotor flux so that the prediction is also improved and the ripples content is decreased and this will be investigated in the following sections.

V. COST EFFECTIVE ROTOR CURRENT ESTIMATION PROCEDURE

As an attempt to save the cost of using two rotor current sensors, a cost effective technique is utilized which enables the calculation of the rotor currents using only one current sensor. The previous introduced current estimation techniques with induction machine (IM) drives as stated in [30]–[33] have depended on varying the hardware configuration for the voltage source inverter (VSI) so that the DC link current and the switching states can be used to reconstruct the three phase currents using one current sensor which is the DC link current sensor.

The drawbacks of these techniques are obvious through utilizing a modulation index with a low value and through the existence of a phase shift during the reconstruction process which can impose an error in the estimated currents.

In order to avoid these shortages, the paper introduces a simple and cost effective technique to estimate the rotor current without making a reconfiguration in the VSI toplogy. To illustrate the base principle upon which the rotor currents are calculated using the proposed technique, the space vector representation shown in Figure 5 is utilized.

In the rotor reference frame, the rotor currents are measurable and can be obtained directly with two current sensors; one of them measure phase 'a' rotor current i^r_{ar} which is the same of α-component current $i^r_{\alpha r}$ as illustrated in Figure 5. In addition, in order to estimate the β-axis component of rotor the current $i^r_{\beta r}$, the second current sensor is used to measure the phase 'b' rotor current i^r_{br} and then the third phase 'c' current i^r_{cr} is calculated and via Clarke transformation, the β-component $i^r_{\beta r}$ is calculated.

On the other hand, the proposed current estimation technique only calculates the α-component current $i^r_{\alpha r}$ while the β-component $i^r_{\beta r}$ is calculated with the help of reference d-q components of rotor current i^*_{dr} and i^*_{qr} which supposed to be equal to the actual d-q components of rotor current $i^{\bar{\psi}_s}_{dr}$ and $i^{\bar{\psi}_s}_{qr}$. This can be explained as follows:

From Figure 5, and along the q^r- axis of the rotor frame, the projections of the reference rotor current d-q components i^*_{dr} and i^*_{qr} are given by

$$i^*_{dr} \sin\left(\theta_{\bar{\psi}_s} - \hat{\theta}_{me}\right), \quad \text{and } i^*_{qr} \cos\left(\theta_{\bar{\psi}_s} - \hat{\theta}_{me}\right) \tag{33}$$

By vector summation, the two parts of (33) gives the β-component of rotor current $i^r_{\beta r}$ by

$$\hat{i}^r_{\beta r} = i^*_{dr} \sin\left(\theta_{\bar{\psi}_s} - \hat{\theta}_{me}\right) + i^*_{qr} \cos\left(\theta_{\bar{\psi}_s} - \hat{\theta}_{me}\right) \tag{34}$$

where the superscript ^ is used to state that the current is estimated and not directly measured. Moreover, the rotor current references i^*_{dr} and i^*_{qr} are obtained using (10).

The obtained formulation of (34) can be also validated mathematically as follows:

The stator voltage vector in stationary frame can be expressed at instant kT_s by

$$\bar{u}^s_{s,k} = R_s \bar{i}^s_{s,k} + \frac{d\bar{\psi}^s_{s,k}}{dt} \tag{35}$$

While, it can represented in rotor frame by

$$\bar{u}^r_{s,k} = \bar{u}^s_{s,k} e^{-j\hat{\theta}_{me,k}} = R_s \bar{i}^s_{s,k} e^{-j\hat{\theta}_{me,k}} + \frac{d\bar{\psi}^s_{s,k}}{dt} e^{-j\hat{\theta}_{me,k}} \tag{36}$$

The relationship (36) can be reformulated to be expressed by

$$\begin{aligned} \bar{u}^r_{s,k} &= \bar{u}^r_{\alpha s,k} + j\bar{u}^r_{\beta s,k} \\ &= R_s \left(\bar{i}^r_{\alpha s,k} + j\bar{i}^r_{\beta s,k}\right) \\ &\quad + \frac{d\left(\bar{\psi}^r_{\alpha s,k} + j\bar{\psi}^r_{\beta s,k}\right)}{dt} \\ &\quad - \hat{\omega}_{me,k}\left(\bar{\psi}^r_{\beta s,k} - j\bar{\psi}^r_{\alpha s,k}\right) \end{aligned} \tag{37}$$

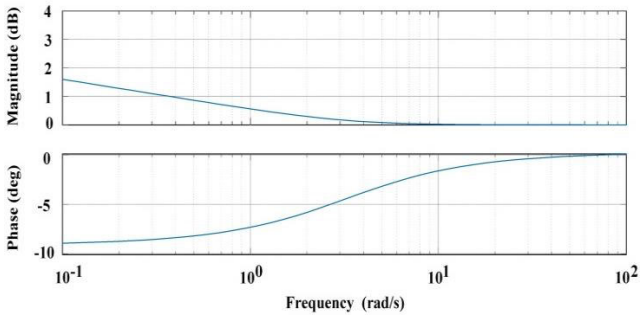

FIGURE 7. Performance of voltage model based rotor flux observer with a 50% mismatch in stator resistance.

By taking the imaginary part of (37), this results

$$\bar{u}^r_{\beta s,k} = R_s \bar{i}^r_{\beta s,k} + \frac{d\bar{\psi}^r_{\beta s,k}}{dt} + \hat{\omega}_{me,k}\bar{\psi}^r_{\alpha s,k} \tag{38}$$

And via utilizing the flux and current relationships, (38) tends to be

$$\bar{u}^r_{\beta s,k} = R_s\left[\frac{\psi^r_{\beta s,k} - L_m i^r_{\beta r,k}}{L_s}\right] + \frac{d\bar{\psi}^r_{\beta s,k}}{dt} + \hat{\omega}_{me,k}\bar{\psi}^r_{\alpha s,k} \tag{39}$$

From Figure 5, it is obvious that

$$\begin{aligned}\bar{\psi}^r_{\alpha s,k} &= \left|\bar{\psi}^{sf}_{s,k}\right| \cos\left(\theta_{\bar{\psi}_{s,k}} - \hat{\theta}_{me,k}\right), \quad \text{and} \\ \bar{\psi}^r_{\beta s,k} &= \left|\bar{\psi}^{sf}_{s,k}\right| \sin\left(\theta_{\bar{\psi}_{s,k}} - \hat{\theta}_{me,k}\right)\end{aligned} \tag{40}$$

By substituting from (40) into (39), it results

$$\begin{aligned}\bar{u}^r_{\beta s,k} = &\frac{\left|\bar{\psi}^{sf}_{s,k}\right| \sin\left(\theta_{\bar{\psi}_{s,k}} - \hat{\theta}_{me,k}\right)}{\left(L_s/R_s\right)} - \frac{L_m i^r_{\beta r,k}}{\left(L_s/R_s\right)} \\ &+ \frac{d\left(\left|\bar{\psi}^{sf}_{s,k}\right| \sin\left(\theta_{\bar{\psi}_{s,k}} - \hat{\theta}_{me,k}\right)\right)}{dt} \\ &+ \hat{\omega}_{me,k}\left|\bar{\psi}^{sf}_{s,k}\right| \cos\left(\theta_{\bar{\psi}_{s,k}} - \hat{\theta}_{me,k}\right)\end{aligned} \tag{41}$$

The stator flux can be defined in terms of magnetizing current by $\bar{\psi}^{sf}_{s,k} \cong \psi^{sf}_{ds,k} = L_m i^{sf}_{d\_m,k}$, and via substituting in (41), the estimated β-component $\hat{i}^r_{\beta r,k}$ can be calculated by

$$\begin{aligned}\hat{i}^r_{\beta r,k} = &-\frac{\bar{u}^r_{\beta s,k}}{L_m}\frac{L_s}{R_s} + \omega_{\bar{\psi}_{s,k}} i^{sf}_{d_m,k} \cos\left(\theta_{\bar{\psi}_{s,k}} - \hat{\theta}_{me,k}\right) \\ &+ \left(i^{sf}_{d\_m,k} + \frac{L_s}{R_s}\frac{di^{sf}_{d\_m,k}}{dt}\right) \sin\left(\theta_{\bar{\psi}_{s,k}} - \hat{\theta}_{me,k}\right)\end{aligned} \tag{42}$$

The relationship between the magnetizing current $\bar{i}^{sf}_{m,k}$ and stator voltage and rotor current defined along the d-axis of the synchronous rotating can be expressed after some derivations by

$$\frac{L_s}{R_s}\frac{di^{sf}_{d\_m,k}}{dt} + i^{sf}_{d\_m,k} = \frac{\bar{u}^{sf}_{ds,k}}{R_s}(1+\sigma_s) + i^{sf}_{dr,k} \tag{43}$$

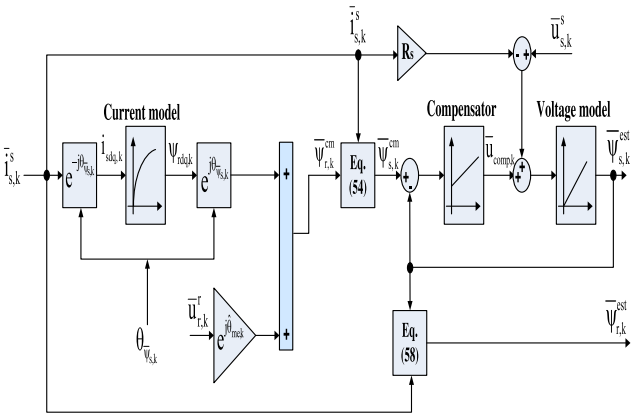

FIGURE 8. Stator and rotor flux estimator.

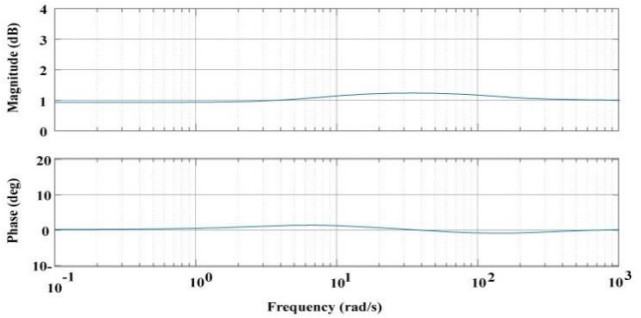

FIGURE 9. Performance of proposed rotor flux observer with a 50% mismatch in stator resistance.

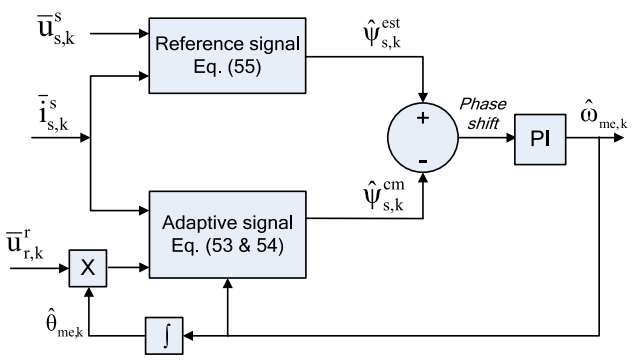

FIGURE 10. Rotor speed and position observer using the improved estimated flux signal.

where σ_s is the stator leakage coefficient. Moreover, from the stator voltage equation, the synchronous angular frequency $\omega_{\bar{\psi}_{s,k}}$ is given by

$$\omega_{\bar{\psi}_{s,k}} = \frac{\bar{u}^{sf}_{qs,k}}{L_m i^{sf}_{d\_m,k}} - \frac{i^{sf}_{qr,k}}{\left(L_s/R_s\right) i^{sf}_{d\_m,k}} \tag{44}$$

where

$$i^{sf}_{qr,k} = \frac{-L_s}{L_m} i^{sf}_{qs,k}, \quad \text{and } i^{sf}_{d\_m,k} = \frac{L_s}{L_m} i^{sf}_{ds,k} + i^{sf}_{dr,k} \tag{45}$$

Now, via substituting from (43) and (44) into (42), and by replacing $i^{sf}_{dr,k}$ and $i^{sf}_{qr,k}$ with their references $i^*_{dr,k}$ and $i^*_{qr,k}$,

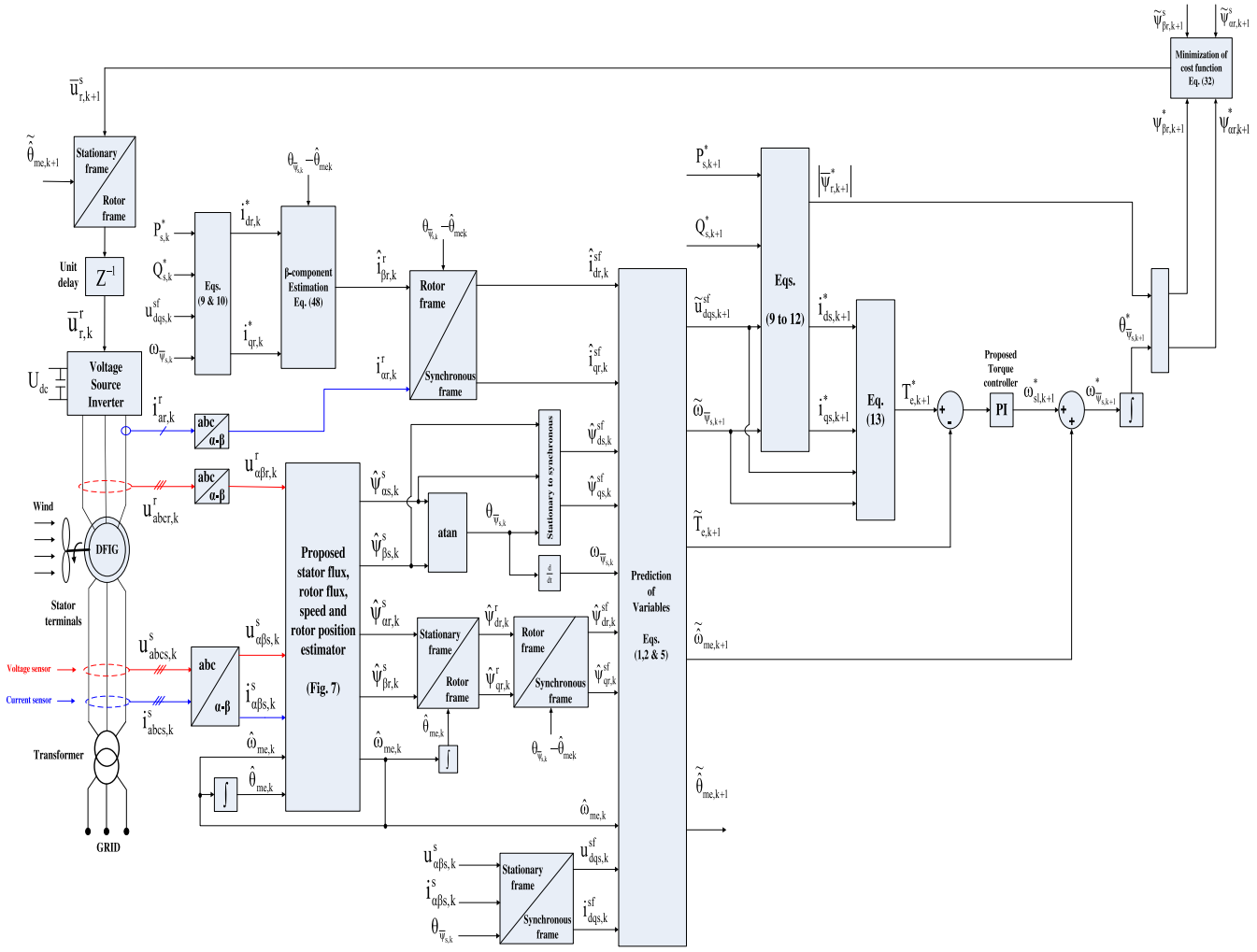

FIGURE 11. Proposed predictive flux control (PFC) overall configuration.

it results

$$\hat{i}^{r}_{\beta r,k} = -\frac{\bar{u}^{r}_{\beta s,k}}{L_m}\frac{L_s}{R_s} + \frac{L_s}{R_s}\hat{i}^{sf}_{d\_m,k}\cos\left(\theta_{\bar{\psi}_{s,k}} - \hat{\theta}_{me,k}\right) \times \left(\frac{\bar{u}^{sf}_{qs,k}}{L_m\hat{i}^{sf}_{d\_m,k}} - \frac{i^{*}_{qr,k}}{\left(L_s/R_s\right)\hat{i}^{sf}_{d\_m,k}}\right) + \left(\frac{\bar{u}^{sf}_{ds,k}}{R_s}(1+\sigma_s) + i^{*}_{dr,k}\right)\sin\left(\theta_{\bar{\psi}_{s,k}} - \hat{\theta}_{me,k}\right) \quad (46)$$

Then by re-arranging (46), this results in

$$\hat{i}^{r}_{\beta r,k} = -\frac{\bar{u}^{r}_{\beta s,k}}{L_m}\frac{L_s}{R_s} + \frac{L_s}{L_m R_s}\left(\overbrace{\bar{u}^{sf}_{qs,k}\cos\left(\theta_{\bar{\psi}_{s,k}} - \hat{\theta}_{me,k}\right) + \bar{u}^{sf}_{ds,k}\sin\left(\theta_{\bar{\psi}_{s,k}} - \hat{\theta}_{me,k}\right)}^{=\bar{u}^{r}_{\beta s,k}}\right) + \left[i^{*}_{dr,k}\sin\left(\theta_{\bar{\psi}_{s,k}} - \hat{\theta}_{me,k}\right) + i^{*}_{qr,k}\cos\left(\theta_{\bar{\psi}_{s,k}} - \hat{\theta}_{me,k}\right)\right] \quad (47)$$

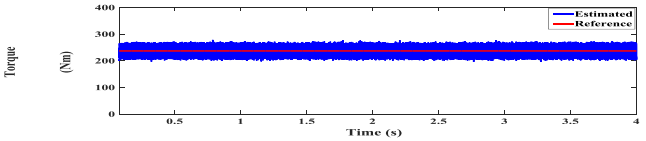

FIGURE 12. Torque under PTC (Sub to super synchronous) (Nm).

Then from (47), it can be concluded that the estimated β-component of rotor current $\hat{i}^{r}_{\beta r,k}$ is given by

$$\hat{i}^{r}_{\beta r,k} = \left[i^{*}_{dr,k}\sin\left(\theta_{\bar{\psi}_{s,k}} - \hat{\theta}_{me,k}\right) + i^{*}_{qr,k}\cos\left(\theta_{\bar{\psi}_{s,k}} - \hat{\theta}_{me,k}\right)\right] \quad (48)$$

which is the same as (34). Figure 6 shows the procedure of rotor current estimation.

VI. PROPOSED ROTOR FLUX AND ROTOR POSITION ESTIMATOR

For improving the rotor flux estimation, a robust stator and rotor fluxes estimator is proposed. It is well recognized that the voltage model $^{(vm)}$ based flux estimators are usually suf-

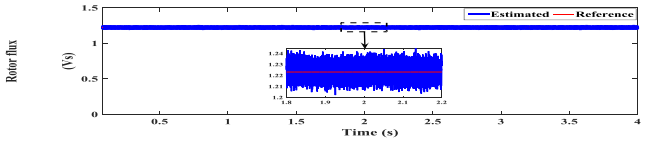

FIGURE 13. Rotor flux under PTC (Sub to super synchronous) (Vs).

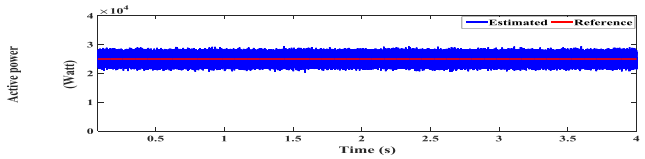

FIGURE 14. Active power under PTC (Sub to super synchronous) (Watt).

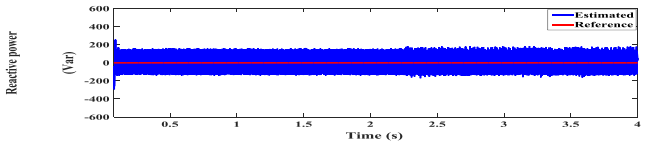

FIGURE 15. Reactive power under PTC (Sub to super synchronous) (Var).

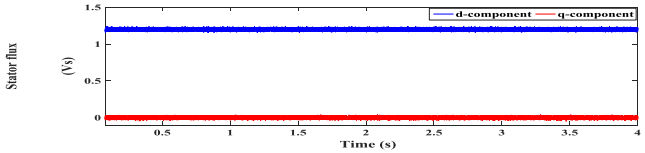

FIGURE 16. Stator flux under PTC (Sub to super synchronous) (Vs).

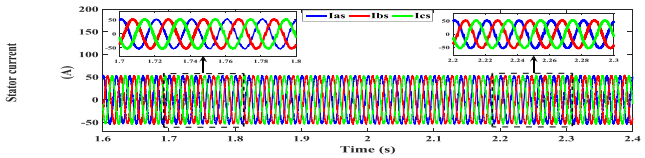

FIGURE 17. Stator currents under PTC (Sub to super synchronous) (A).

fering from multiple issues the low speed operating ranges and this can be referred to many reasons; such as the presence of DC drift in the integrated signal and the sensitivity to parameters variation (specifically stator resistance).

In order to investigate the effect of stator resistance variation on the performance of the voltage model based flux estimator, the transfer function which outlines the dynamic response of the flux estimator is analyzed as follows

In the stationary reference frame $'s'$, the voltage balance in the DFIG can be described by

$$\begin{aligned} \bar{u}^s_{s,k} &= R_s \bar{i}^s_{s,k} + \frac{d\bar{\psi}^s_{s,k}}{dt}, \quad \text{and} \\ \bar{u}^s_{r,k} &= R_r \bar{i}^s_{r,k} + \left(\frac{d}{dt} - j\omega_{me,k}\right)\bar{\psi}^s_{r,k} \end{aligned} \tag{49}$$

From the first relationship in (50), the stator flux can be obtained via integration and then the rotor flux can be estimated by the following expression

$$\hat{\psi}^s_{r,k} = \frac{L_r}{L_m}\hat{\psi}^s_{s,k} - \frac{\sigma L_m}{1-\sigma}\bar{i}^s_{s,k} \tag{50}$$

where $\sigma = 1 - L_m^2/L_r L_s$ is the total leakage factor. Then, by taking the Laplace transform of first relationship in (50)

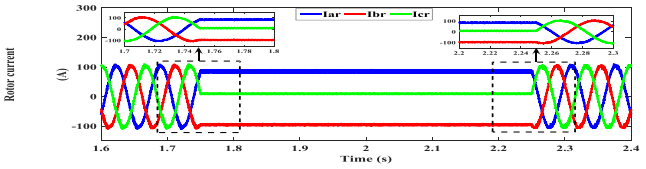

FIGURE 18. Rotor currents under PTC (Sub to super synchronous) (A).

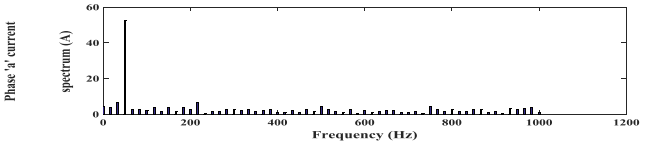

FIGURE 19. Current spectrum under PTC (Sub to super synchronous).

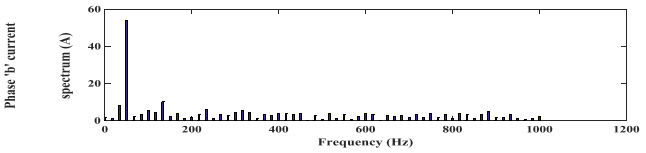

FIGURE 20. Current spectrum under PTC (Sub to super synchronous).

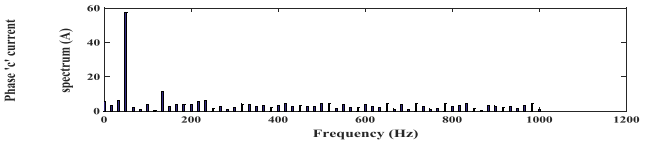

FIGURE 21. Current spectrum under PTC (Sub to super synchronous).

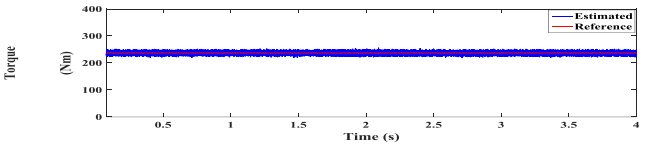

FIGURE 22. Torque under PFC (Sub to super synchronous) (Nm).

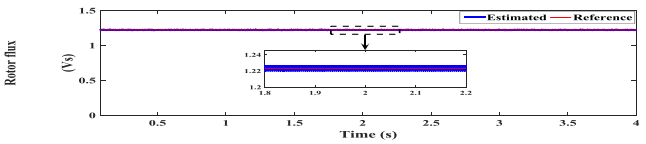

FIGURE 23. Rotor flux under PFC (Sub to super synchronous) (Vs).

and (50) and after the mathematical derivations, the transfer function which outlines the response of the estimated rotor flux respecting to the operating frequency with considering of 50% mismatch in stator resistance can be expressed by

$$\frac{\hat{\psi}^{with\ mismatch}_{r,k}}{\hat{\psi}^{without\ mismatch}_{r,k}} = \left[1 + \frac{L_r^2}{L_m R_r}\left(\frac{R_r}{L_r} + j\omega_{sl,k}\right) * -j\left(\frac{R_s^{actual} - R_s^{mismatched}}{\omega_{sl,k} + \omega_{me,k}}\right)\right] \tag{51}$$

Then, via plotting the bode diagram for (51), it results the frequency response shown in Figure 7 from which it can be realized that the feed forward voltage model based rotor flux estimator is very sensitive to the variation in stator resistance specially at low speed operation. Thus, a mechanism for compensating the resistance mismatch has to be adopted.

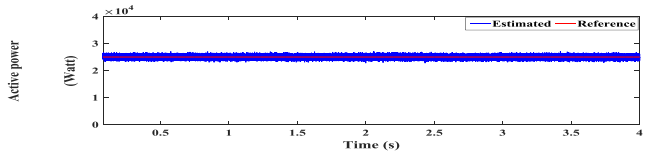

FIGURE 24. Active power under PFC (Sub to super synchronous) (Watt).

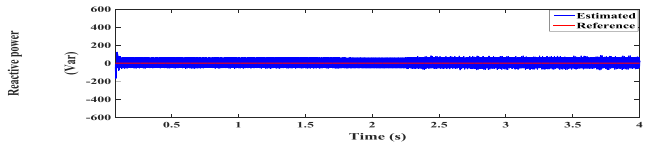

FIGURE 25. Reactive power under PFC (Sub to super synchronous) (Var).

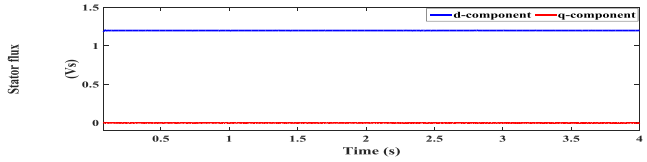

FIGURE 26. Stator flux under PFC (Sub to super synchronous) (Vs).

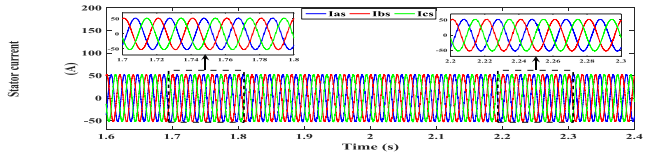

FIGURE 27. Stator currents under PFC (Sub to super synchronous) (A).

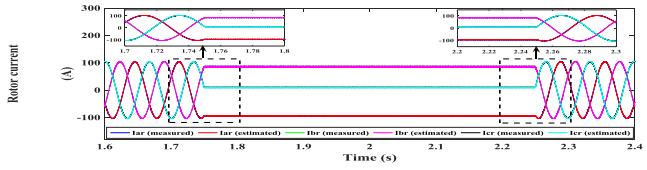

FIGURE 28. Rotor currents under PFC (Sub to super synchronous) (A).

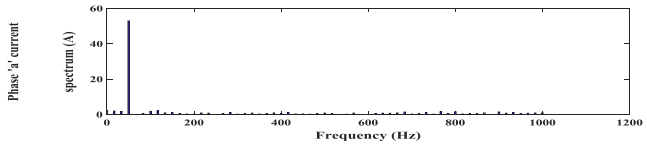

FIGURE 29. Current spectrum under PFC (Sub to super synchronous).

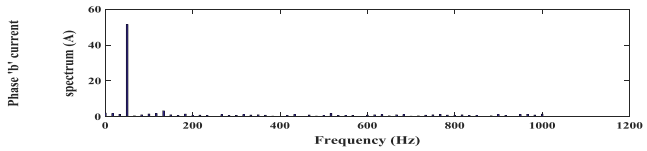

FIGURE 30. Current spectrum under PFC (Sub to super synchronous).

Several stator resistance adaptation mechanisms have been used for the wound rotor type IM [34]–[36], but the proposed adaptation procedures added extra computational burden on the control system and for this reason the rotor flux estimator proposed here is modified to compensate the stator flux estimation error which rises due to the mismatch in R_s value.

The rotor flux can estimated using the current model $^{(cm)}$ of the DFIG which can be derived with the help of second

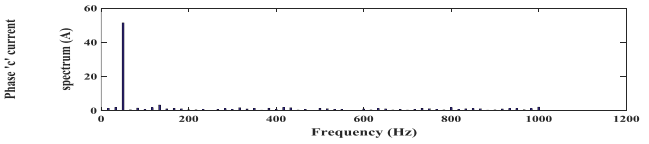

FIGURE 31. Current spectrum under PFC (Sub to super synchronous).

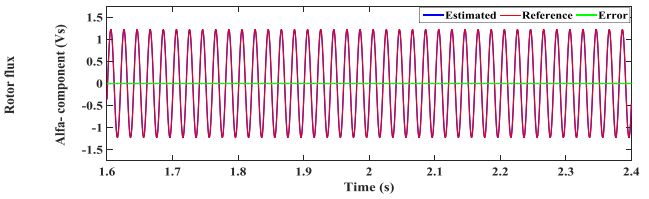

FIGURE 32. Rotor flux α-component for PFC (Sub to super synchronous) (Vs).

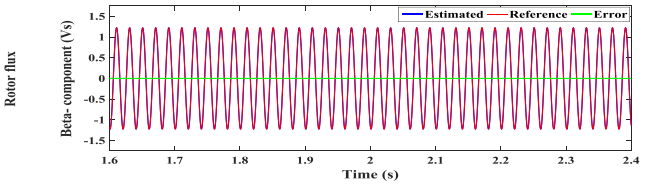

FIGURE 33. Rotor flux β-component for PFC (Sub to super synchronous) (Vs).

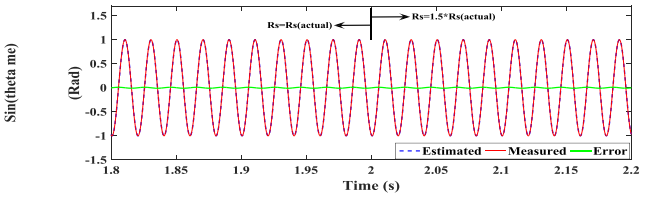

FIGURE 34. Sin(θme) of rotor position for PFC (Sub to super synchronous).

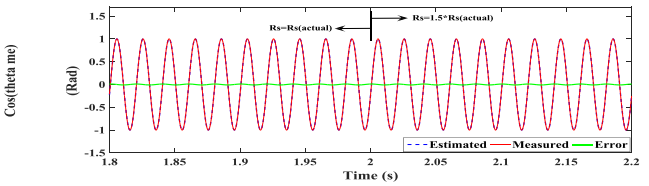

FIGURE 35. Cos(θme) of rotor position for PFC (Sub to super synchronous).

relationship in (50) as follows

$$\hat{\psi}^{cm}_{r,k} = \frac{T_r}{(1+ST_r)}\bar{u}^{s}_{r,k} + \frac{L_m}{(1+ST_r)}\bar{i}^{s}_{s,k} + j\frac{\omega_{me,k}T_r}{(1+ST_r)}\hat{\psi}^{cm}_{r,k} \quad (52)$$

where $T_r = L_r/R_r$ is the rotor time constant, and $\bar{u}^{s}_{r,k} = \bar{u}^{r}_{r,k}e^{\hat{\theta}_{me,k}}$ is the rotor voltage defined in stationary frame with the help of estimated rotor position $\hat{\theta}_{me,k}$.

At low speed operation, the current model is exhibiting better rotor flux estimation compared with the voltage model and thus from (52), the stator flux can be estimated using the current model by

$$\hat{\psi}^{cm}_{s,k} = \frac{L_m}{L_r}\hat{\psi}^{cm}_{r,k} + L_t\bar{i}^{s}_{s,k} \quad (53)$$

The estimation error in the stator flux $\hat{\psi}^{vm}_{s,k}$ obtained by voltage model can be compensated via imposing a compensating

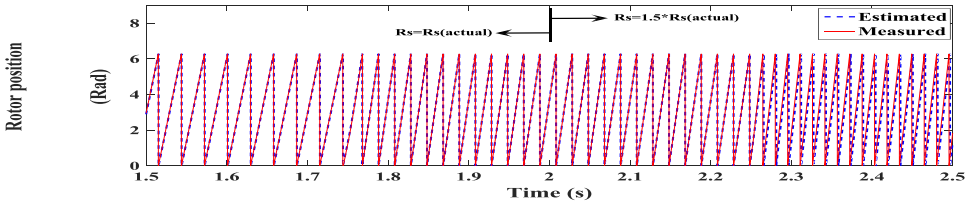

FIGURE 36. Estimated rotor position for PFC (Sub to super synchronous).

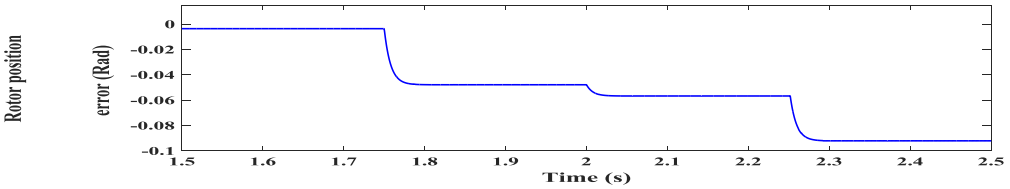

FIGURE 37. Rotor position estimation error for PFC (Sub to super synchronous).

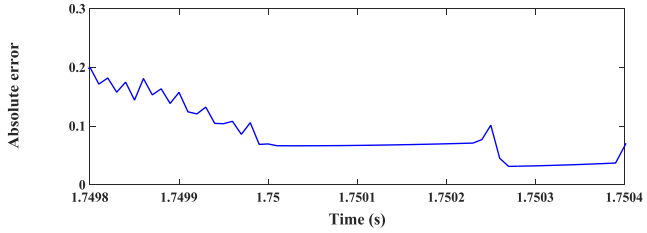

FIGURE 38. Absolute error under PTC (Sub to super synchronous).

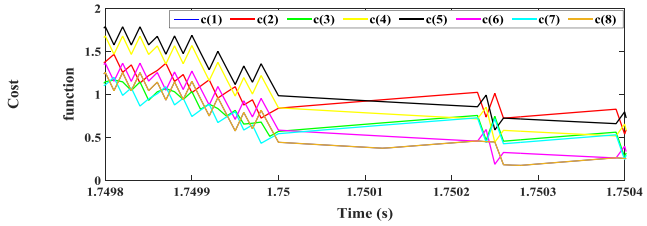

FIGURE 39. Cost function under PTC (Sub to super synchronous).

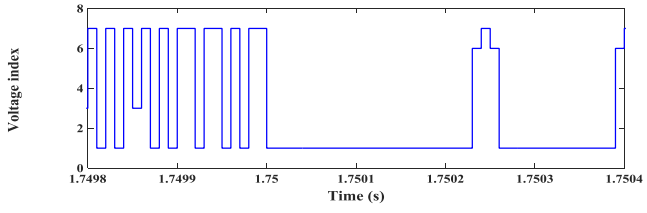

FIGURE 40. Voltage index variation under PTC (Sub to super synchronous).

signal as follows

$$\hat{\psi}^{est}_{s,k} = \frac{1}{s}\left(\bar{u}^{s}_{s,k} - R_s \bar{i}^{s}_{s,k} - \bar{u}_{comp,k}\right) \tag{54}$$

The additional term $\bar{u}_{comp,k}$ is utilized to compensate the estimation error due to R_s variation and due to DC drift. The compensating term $\bar{u}_{comp,k}$ can be evaluated by

$$\bar{u}_{comp,k} = \left(k_p + \frac{k_i}{s}\right)\left(\hat{\psi}^{vm}_{s,k} - \hat{\psi}^{cm}_{s,k}\right) \tag{55}$$

The coefficients of the PI controller in (55) can be determined by identifying the task of each model in the estimator. For

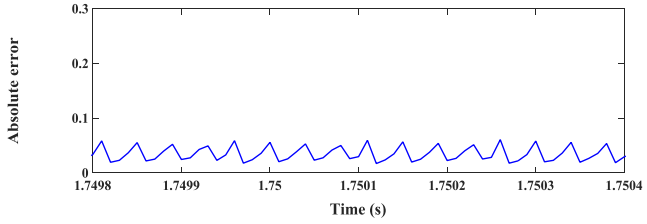

FIGURE 41. Absolute error under PFC (Sub to super synchronous).

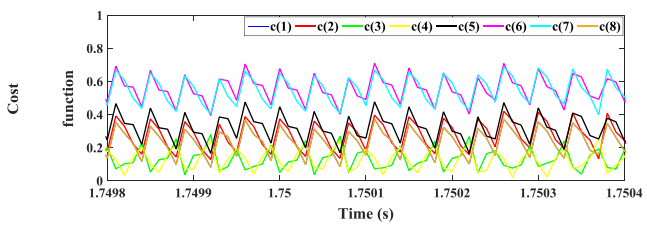

FIGURE 42. Cost function under PTC (Sub to super synchronous).

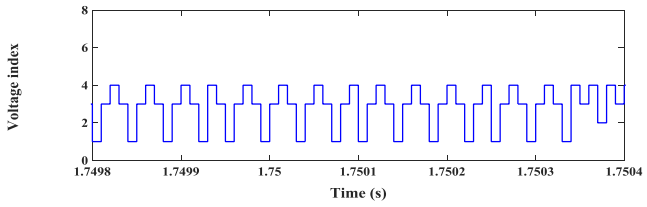

FIGURE 43. Voltage index variation under PTC (Sub to super synchronous).

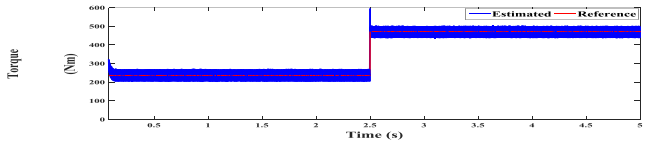

FIGURE 44. Torque under PTC at synchronous speed (Nm).

example, at high speed operation, the voltage model dynamics described by (54) is dominating, while at low speed operation, the current model dynamics described by (53) governs and based on this hypothesis, the PI coefficients are computed

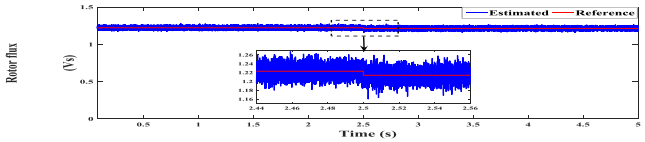

FIGURE 45. Rotor flux under PTC at synchronous speed (Vs).

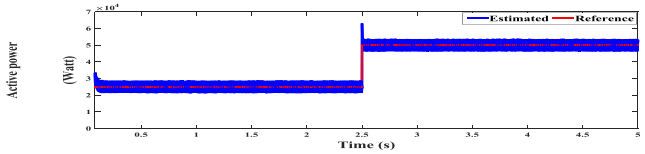

FIGURE 46. Active power under PTC at synchronous speed (Watt).

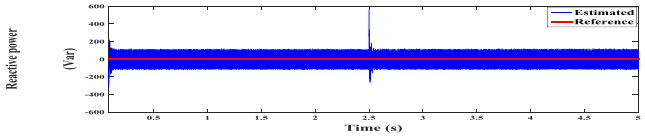

FIGURE 47. Reactive power under PTC at synchronous speed (Var).

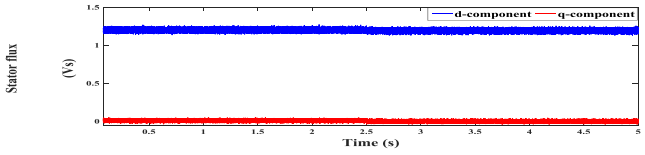

FIGURE 48. Stator flux under PTC at synchronous speed (Vs).

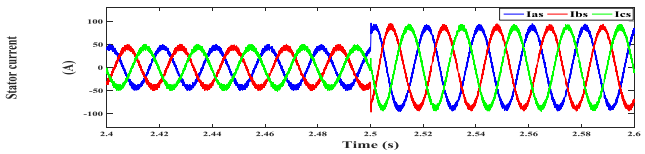

FIGURE 49. Stator currents under PTC at synchronous speed (A).

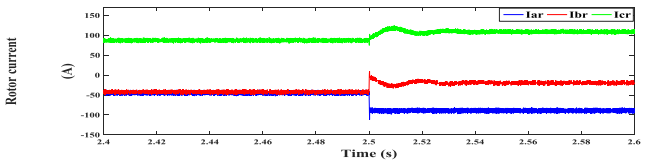

FIGURE 50. Rotor currents under PTC at synchronous speed (A).

by

$$k_p = \omega_1 + \omega_2, \quad \text{and } k_i = \omega_1 * \omega_2 \tag{56}$$

where ω_1 ranges from 1 to 5 rad/s and ω_2 ranges from 10 to 30 rad/s. The selected values of ω_1 and ω_2 are very appropriate to stimulate the possible operating ranges (low speed and high speed). Now, the estimated rotor flux can be evaluated in terms of the estimated stator flux which is calculated with the help of (53), (54) and (55) by

$$\hat{\psi}_{r,k}^{est} = \frac{L_r}{L_m}\hat{\psi}_{s,k}^{est} - L_t \bar{i}_{s,k}^{s} \tag{57}$$

The schematic of the proposed stator and rotor flux estimator is shown in Figure 8 in which the utilized rotor current is obtained via adopting the rotor current estimation procedure presented in Sec.V.

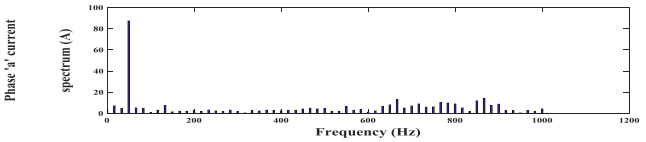

FIGURE 51. Phase 'a' current spectrum under PTC at synchronous speed.

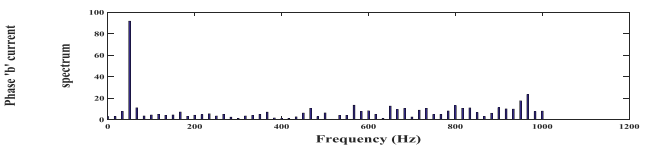

FIGURE 52. Phase 'b' current spectrum under PTC at synchronous speed.

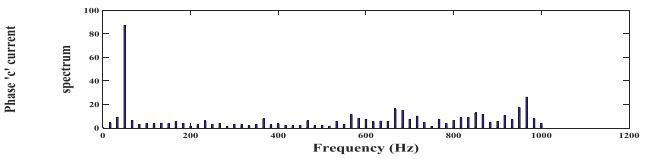

FIGURE 53. Phase 'c' current spectrum under PTC at synchronous speed.

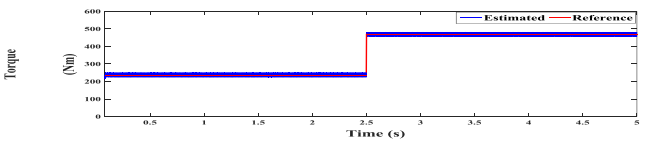

FIGURE 54. Torque under PFC at synchronous speed (Nm).

To investigate the dynamic response of the proposed flux estimator with respect to the operating frequency, the transfer function of the proposed rotor flux estimator considering a mismatch of 50% in R_s is defined by

$$\frac{\hat{\psi}_{r,k}^{withmismatch}}{\hat{\psi}_{r,k}^{withoutmismatch}} = \frac{\left[1+\frac{L_r^2}{L_m R_r}\left(\frac{R_r}{L_r}+j\omega_{sl,k}\right) * -j\left(\frac{R_s^{actual}-R_s^{mismatched}}{\omega_{sl,k}+\omega_{me,k}}\right)\right] * K^{comp}}{\frac{L_m}{L_r} * \frac{d}{dt} + K^{comp}} \tag{58}$$

where K^{comp} refers to the linear state feedback compensator. Now to check the robustness of the proposed flux estimator the bode plot of (58) is presented in Figure 9 which reports that the proposed flux estimator is robust against the R_s variation which enhance the stator flux and rotor flux estimation as well.

After verifying the validity and robustness of the proposed flux estimator, the estimated stator flux $\hat{\psi}_{s,k}^{est}$ which is obtained in stationary frame is considered as a reference signal and the stator flux obtained by the current model $\hat{\psi}_{s,k}^{cm}$ is considered as an adaptive signal (as it is function of estimated speed see (53 & 54)) which are utilized to extract the speed $\hat{\omega}_{me,k}$ and position $\hat{\theta}_{me,k}$ of the rotor through using a PI controller which regulate the phase difference between the positions of the two vectors (reference and adaptive) as shown in Figure 10.

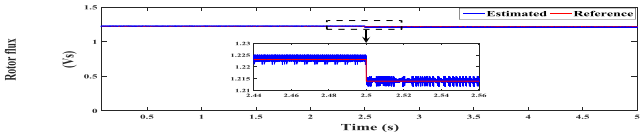

FIGURE 55. Rotor flux under PFC at synchronous speed (Vs).

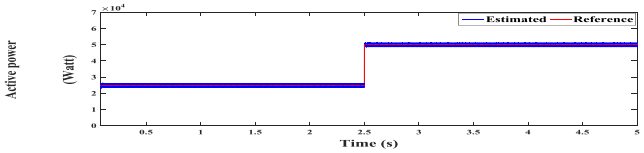

FIGURE 56. Active power under PFC at synchronous speed (Watt).

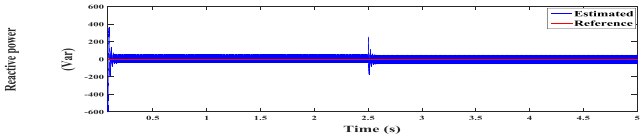

FIGURE 57. Reactive power under PFC at synchronous speed (Var).

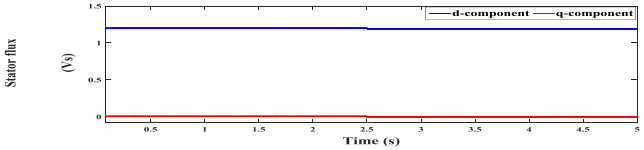

FIGURE 58. Stator flux under PFC at synchronous speed (Vs).

In Figure 10, the phase shift between the vector allocations of the stator flux signals can be calculated by

$$Phaseshift = \psi^{cm}_{\alpha s,k}\hat{\psi}^{est}_{\beta s,k} - \psi^{cm}_{\beta s,k}\hat{\psi}^{est}_{\alpha s,k} \tag{59}$$

Till now, the complete system components are obtained and then the system configuration is layouted in Figure 11.

The cost function terms are calculated and computed in the stationary frame (α-β) and thus the selected rotor voltage $\bar{u}^{s}_{r,k+1}$ which minimizes this function is transformed to the rotor frame with the help of estimated rotor position $\tilde{\theta}_{me,k+1}$ to get the rotor voltage vector $\bar{u}^{r}_{r,k+1}$ which is then delayed by a sampling time T_s to be applied to the rotor terminals at instant kT_s.

It can be also noticed that only one rotor current sensor is utilized to measure the phase 'a' rotor current $i^{r}_{ar,k}$ and calculate the α-component $i^{r}_{\alpha r,k}$ using Clarke transformation, while the β-component $\hat{i}^{r}_{\beta r,k}$ is estimated using the proposed rotor current estimation technique described in Sec. V.

VII. TEST RESULTS

A. SUB-SYNCHRONOUS AND SUPER-SYNCHRONOUS OPERATION

In order to validate the effectiveness of the proposed PFC approach and the robustness of the proposed rotor flux and rotor position estimators against system uncertainties such as the variation of stator resistance R_s, extensive tests have been carried out for a wide speed range. The proposed PFC is tested firstly when changing the DFIG rotational speed from sub-synchronous (from t = 0 s to t = 1.75 s) to super-synchronous operation (from t = 2.25 s to t = 4 s)

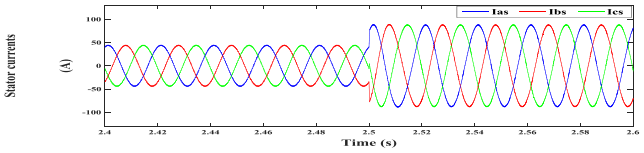

FIGURE 59. Stator currents under PFC at synchronous speed (A).

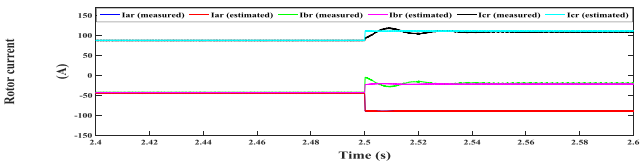

FIGURE 60. Rotor currents under PFC at synchronous speed (A).

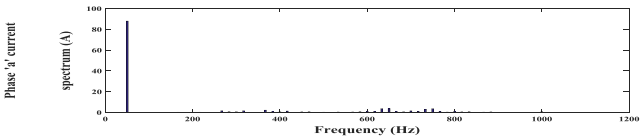

FIGURE 61. Phase 'a' current spectrum under PFC at synchronous speed.

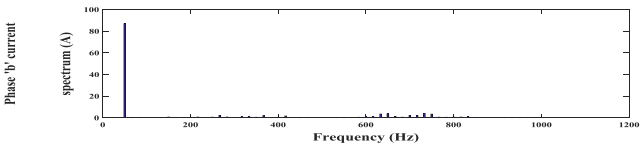

FIGURE 62. Phase 'b' current spectrum under PFC at synchronous speed.

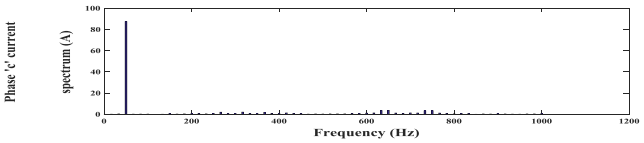

FIGURE 63. Phase 'c' current spectrum under PFC at synchronous speed.

passing through the synchronous operation (from t = 1.75 s to t = 2.25 s). The second test is carried out for operating the DFIG at synchronous speed which is considered as a sensitive operating condition especially for the sensorless estimate. The third test is carried out at very low speed (about 1% of the synchronous speed). The dynamic performance of the sensorless PFC is compared with the dynamic performance of the predictive torque control (PTC) approach.

The first test is performed when varying the speed from sub-synchronous (-30 % of synchronous speed) to synchronous and then to super-synchronous (+30 % of synchronous speed), while keeping the generated active power at 25 Kw and the generated active power at zero value to realize a unity power factor operation. The torque reference value for both of the proposed PFC and PTC approaches is derived using (13), while the rotor flux reference is calculated using (12). For the proposed PFC approach, the reference values of the rotor flux (α-β) components $\psi^{*}_{\alpha r,k+1}$ and $\psi^{*}_{\beta r,k+1}$ are calculated using the designed PI torque controller.

The obtained results show the effectiveness of the proposed PFC in achieving the control target in maintaining the

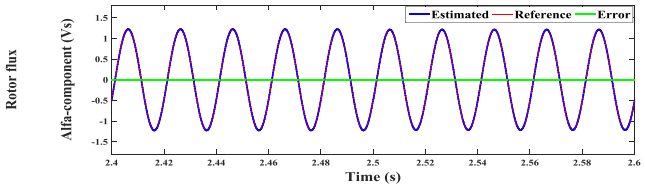

FIGURE 64. Rotor flux α-component under PFC at synchronous speed (Vs).

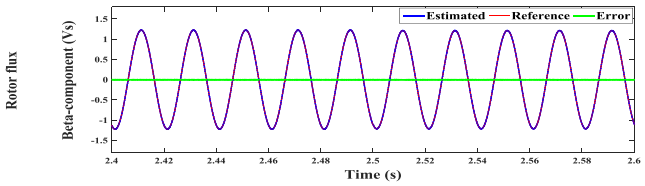

FIGURE 65. Rotor flux β-component under PFC at synchronous speed (Vs).

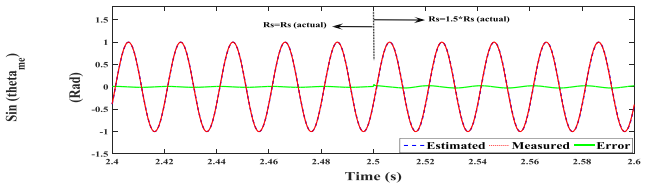

FIGURE 66. Sin(θme) of rotor position under PFC at synchronous speed.

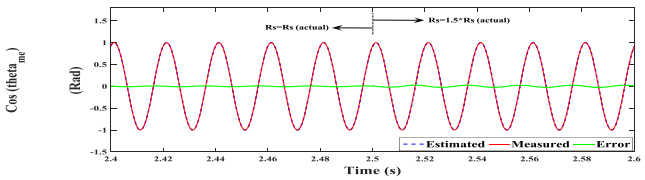

FIGURE 67. Cos(θme) of rotor position under PFC at synchronous speed.

generated active and reactive powers at their references when changing the DFIG operation mode from sub-synchronous to super-synchronous passing therough the synchronous operation which is investigated more in the nest section.

This can be confirmed through Figures 24 and 25, which show that under the PFC the calculated values of active and reactive powers present less ripples content compared with their values obtained under the PTC as shown in Figures 14 and 15. Moreover, the calculated values of torque, rotor flux, stator flux, stator and rotor currents under the proposed PFC exhibit better performance with less harmonics compared with the PTC values as shown in Figures 22, 23, 26, 27 and 28, respectively.

The investigation of the ripples content in the stator currents profiles can be clarified more about performing a Fast Fourier Transform (FFT) analysis for the currents, from which the harmonics are calculated under the two control procedures and then are addressed in the Table 1.

Moreover, the FFT analysis is shown graphically for the two control procedures as illustrated by Figures 19, 20 and 21 for the PTC, and by Figures 29, 30 and 31 for the proposed PFC, and from which the effectiveness of the proposed PFC is confirmed. The actual and reference values of rotor flux (α-β) components under the PFC are presenting high matching degree, which prove the validity of the proposed PFC in

TABLE 1. Stator currents fft for PTC and proposed PFC (sub-synchronous to super-synchronous operation).

	PTC		Proposed PFC	
	Fundamental	THD	Fundamental	THD
Phase 'a'	52.6242 A	16.37 %	53.1377 A	6.03 %
Phase 'b'	53.7682 A	20.31%	51.5338 A	5.92 %
Phase 'c'	57.4956 A	18.69%	51.4465 A	6.82 %

achieving the control objectives with minimum deviations as shown in Figures 32 and 33.

The feasibility of the proposed flux and rotor position observers is confirmed therough the obtained results in Figures 34 and 35 which show the estimated values of the unit vectors ($Sin(\theta_{me})$ and $Cos(\theta_{me})$) of the rotor position which are tracking precisely their correspondant measured values.

The estimated rotor position is also illustrated through Figure 36 which present high degree of a greement with the measured position; this can be confirmed also through checking the estimation error in Figure 37 which has a very small values and can be neglected.

The number of commutaions for the two control procedures is also calculated with the help of computation mechanism shown in Figure 4, and the results are given in table 2, through which it can be realized that the proposed PFC is exhibiting lower computational burden than the PTC which results in reducing the switching losses.

In order to show the detailed behavior of the control action taken by the two control procedures, the instantaneous variation of the absolute error values with respect to the cost function values and voltage vector index is presented. The absolute error for the PTC approach is calculated by

$$|\bar{e}_{k+1}| = \sqrt{\left(\frac{T^*_{e,k+1} - \tilde{T}_{e,k+1}}{T_{rated}}\right)^2 + \left(\frac{\psi^*_{r,k+1} - \tilde{\psi}_{r,k+1}}{\psi_{rated}}\right)^2} \tag{60}$$

While for the proposed PFC, the absolute error is given by

$$|\bar{e}_{k+1}| = \sqrt{\left(\frac{\psi^*_{\alpha r,k+1} - \tilde{\psi}_{\alpha r,k+1}}{\psi_{rated}}\right)^2 + \left(\frac{\psi^*_{\beta r,k+1} - \tilde{\psi}_{\beta r,k+1}}{\psi_{rated}}\right)^2} \tag{61}$$

For the proposed PFC, the Figures 41, 42 and 43 show a remarkable reduction in the average error values when compared with their correspondant ones in Figures 38, 39 and 40 for the PTC. The average value for the absolute error under the PFC is 0.038 while for the PTC is 0.16.

B. TESTING AT SYNCHRONOUS SPEED

The second test is carried out for active power references of 25 Kw and 50 Kw applied at times t = 0 s and t = 2.5 s, respectively. While the reactive power reference value is set to 0.0 Var to realize unity power factor operation. The rotor is driven at the synchronous speed. The rotor position for the PTC approach is measured while it is estimated for the proposed PFC.

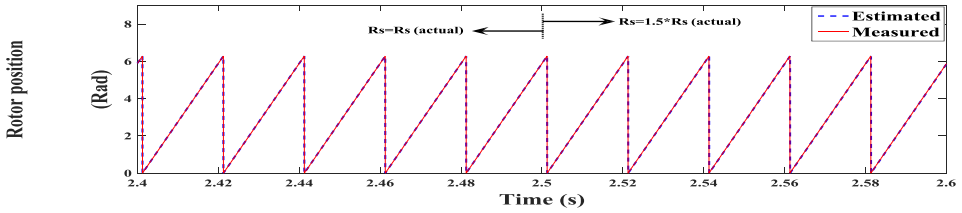

FIGURE 68. Estimated rotor position under PFC at synchronous speed.

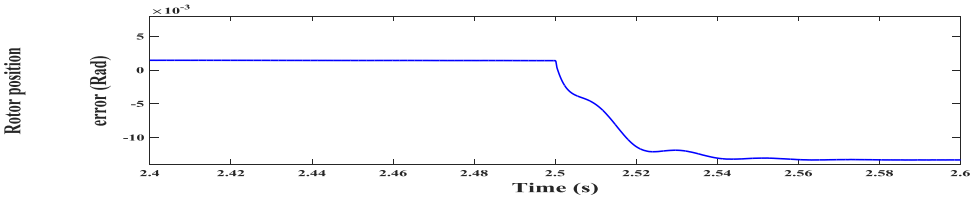

FIGURE 69. Rotor position estimation error under PFC at synchronous speed.

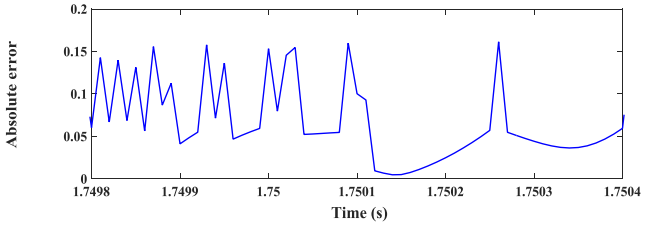

FIGURE 70. Absolute error under PTC at synchronous speed.

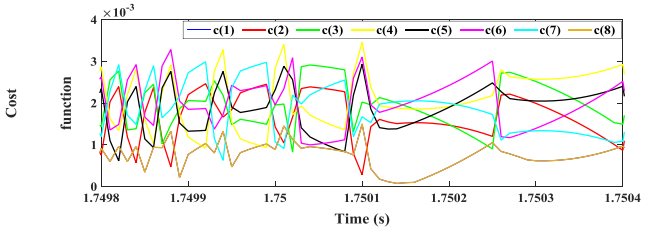

FIGURE 71. Cost function under PTC at synchronous speed.

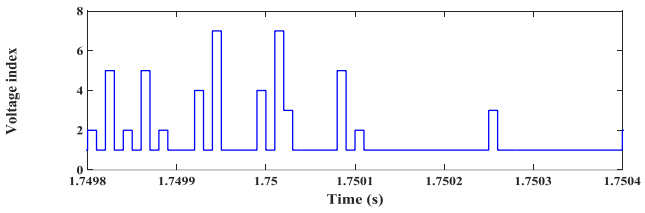

FIGURE 72. Voltage index variation under PTC at synchronous speed.

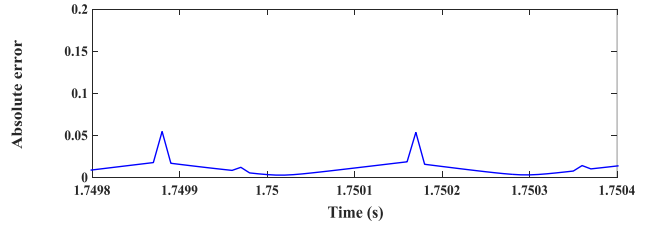

FIGURE 73. Absolute error under PFC at synchronous speed.

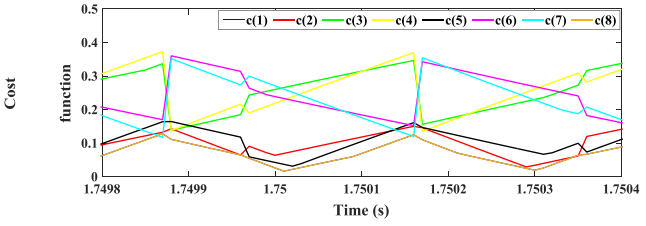

FIGURE 74. Cost function under PFC at synchronous speed.

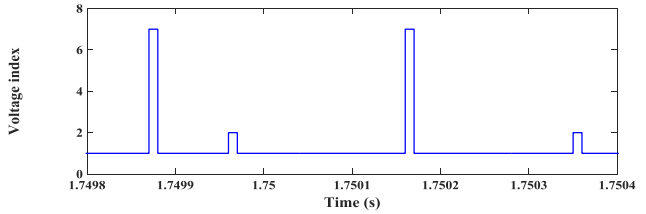

FIGURE 75. Voltage index variation under PFC at synchronous speed.

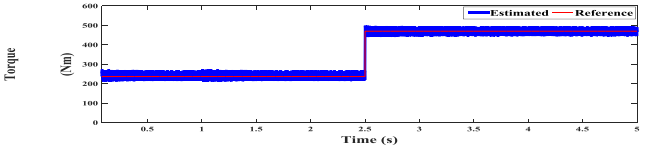

FIGURE 76. Torque under PTC at low speed (Nm).

The obtained results for the proposed PFC show a noticeable ripple reduction in the controlled variables (torque, rotor flux, active and reactive powers, stator flux, stator and rotor currents) which are shown in Figures 54, 55, 56, 57, 58, 59 and 60, respectively. While the correspondent results which are obtained under the PTC and shown through Figures 44, 45, 46, 47, 48, 49 and 50 are presenting higher ripples content. The effectiveness of the proposed PFC in limiting the accompanied noise can be more investigated through applying a FFT analysis to the stator currents under the two control procedures.

The FFT analysis of the stator currents is addressed in Table 1 which demonstrate that the total harmonic distortion (THD) of stator currents under the PFC is with lower values compared with its corresponding values under the

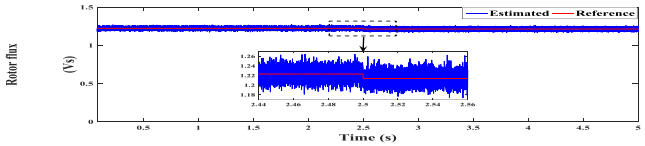

FIGURE 77. Rotor flux under PTC at low speed (Vs).

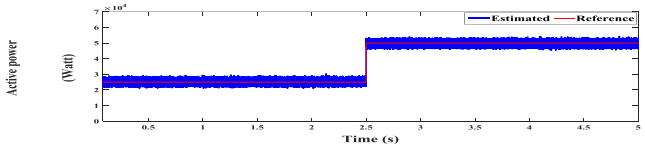

FIGURE 78. Active power under PTC at low speed (Watt).

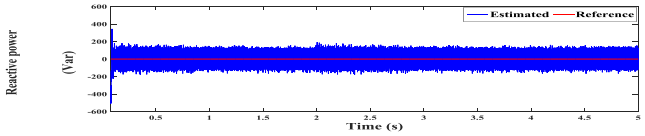

FIGURE 79. Reactive power under PTC at low speed (Var).

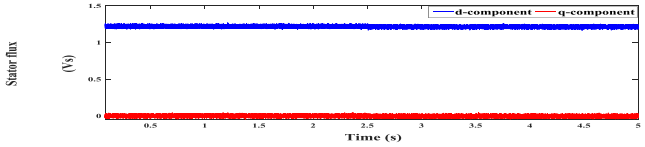

FIGURE 80. Stator flux under PTC at low speed (Vs).

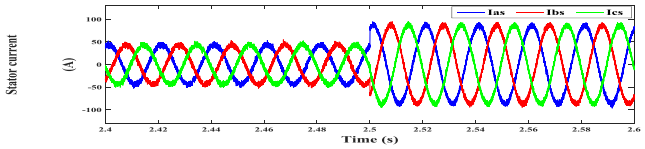

FIGURE 81. Stator currents under PTC at low speed (A).

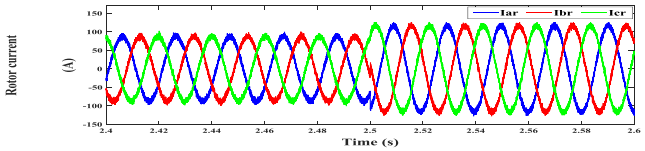

FIGURE 82. Rotor currents under PTC at low speed (A).

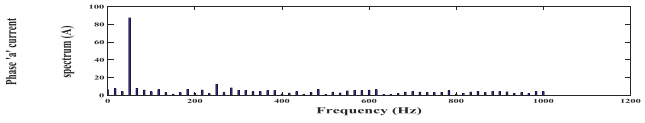

FIGURE 83. Phase 'a' current spectrum under PTC at low speed.

PTC. Moreover, the FFT analysis of phases 'a', 'b' and 'c' of stator current is given for the PTC and PFC approaches in a graphical form as shown through Figures 51, 52 and 53 for the PTC and 61, 62 and 63 for the PFC, respectively. From the presented figures, the ability of the proposed PFC in limiting the accompanied noise in a better way than the PTC approach performs is verified. Table 3 presents an analytical comparison between the harmonics content in the stator currents under the PTC and proposed PFC approaches.

In addition, it can be noticed that the rotor currents exhibit less distortion under the PFC, and they are with zero frequency (DC quantities) due to the zero slip frequency at synchronous speed operation (see Figure 60). Through the same figure, the cost effective rotor current estimation procedure

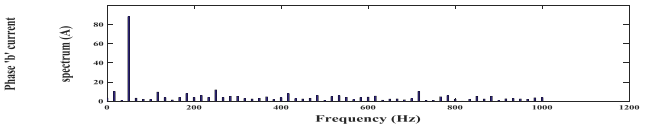

FIGURE 84. Phase 'b' current spectrum under PTC at low speed.

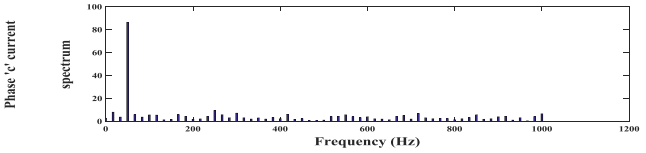

FIGURE 85. Phase 'c' current spectrum under PTC at low speed.

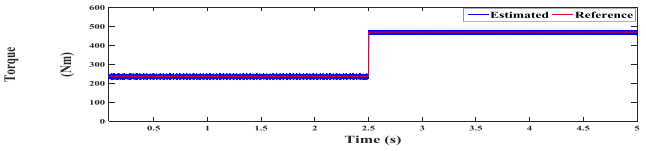

FIGURE 86. Torque under PFC at low speed (Nm).

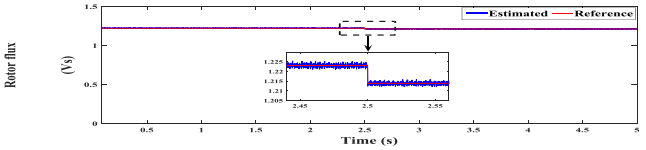

FIGURE 87. Rotor flux under PFC at low speed (Vs).

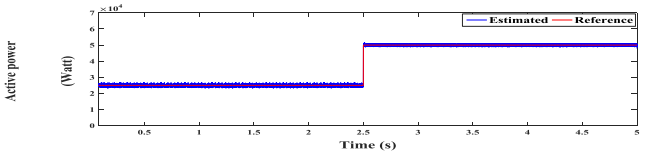

FIGURE 88. Active power under PFC at low speed (Watt).

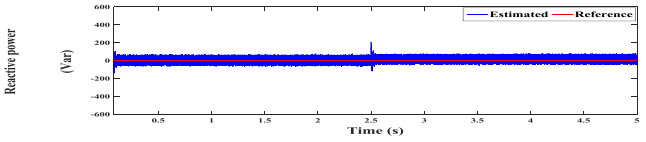

FIGURE 89. Reactive power under PFC at low speed (Var).

TABLE 2. Number of commutations (sub-synchronous to super-synchronous operation).

	PTC	Proposed PFC
COMMUTATIONS	7513	4213
SWITCHING FREQUENCY	1.25 KHz	702 Hz

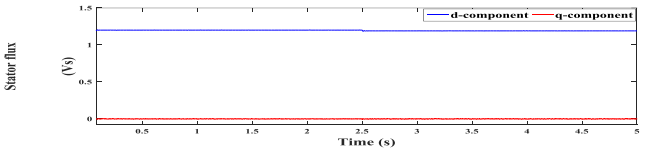

FIGURE 90. Stator flux under PFC at low speed (Vs).

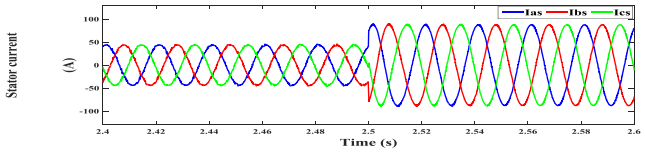

FIGURE 91. Stator currents under PFC at low speed (A).

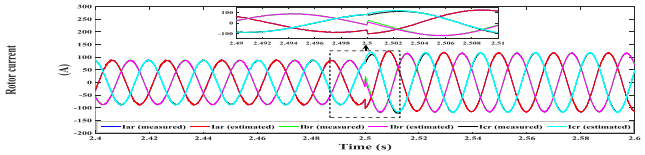

FIGURE 92. Rotor currents under PFC at low speed (A).

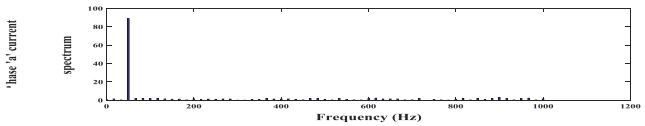

FIGURE 93. Phase 'a' current spectrum under PFC at low speed.

TABLE 3. Stator currents FFT for PTC and proposed PFC at synchronous speed.

	PTC		Proposed PFC	
	Fundamental	THD	Fundamental	THD
Phase 'a'	87.508 A	20.35 %	88.0384 A	6.85 %
Phase 'b'	91.8518 A	25.22%	87.2173 A	7.94 %
Phase 'c'	87.3916 A	18.46%	87.4552 A	6.33 %

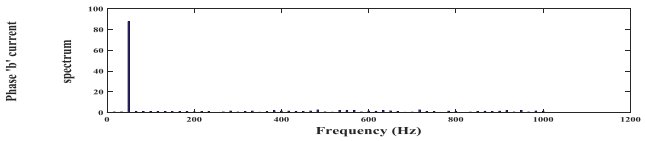

FIGURE 94. Phase 'b' current spectrum under PFC at low speed.

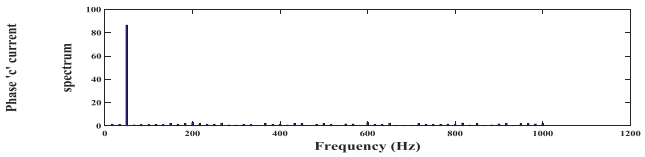

FIGURE 95. Phase 'c' current spectrum under PFC at low speed.

is confirming its feasibility through the precise estimation of rotor current.

Moreover, the proposed sensroless scheme is confirming its effectiveness through the precise estimation of rotor position even with a mismatch in the stator resistance of 50% applied at time t = 2.5s; this can be investigated through the observed minimum deviation from the measured values as shown in Figures 66 and 67 which demonstrate the estimated and actual unit vectors (*sin* and *cos*) of the rotor position. In Figure 68, the estimated rotor position tracks precisely the actual position even with a variation in the stator resistance which confirms the robustness of the proposed sensorless procedure. This can be reconfirmed through the position estimation error which is almost zero as shown in Figure 69.

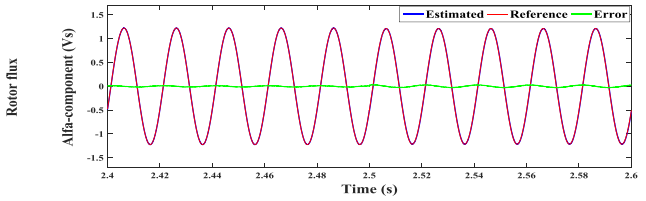

FIGURE 96. Rotor flux α-component under PFC at low speed (Vs).

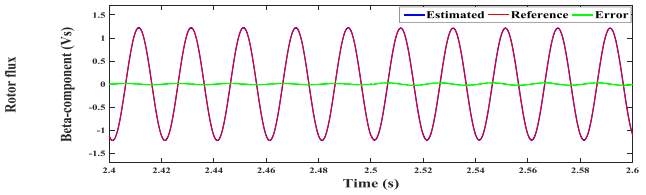

FIGURE 97. Rotor flux β-component under PFC at low speed (Vs).

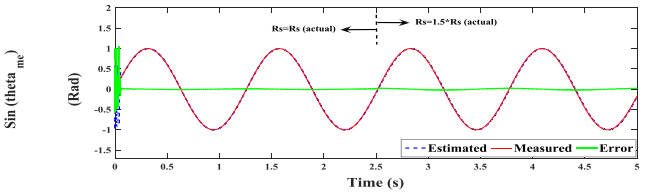

FIGURE 98. Sin(θme) of rotor position under PFC at low speed.

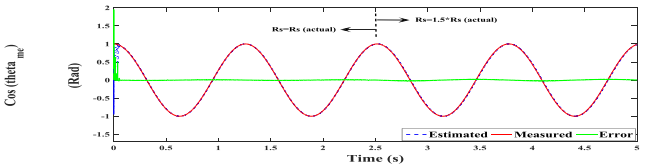

FIGURE 99. Cos(θme) of rotor position under PFC at low speed.

TABLE 4. Number of commutations at synchronous speed.

	PTC	Proposed PFC
COMMUTATIONS	7246	4376
SWITCHING FREQUENCY	1.2 KHz	729 Hz

Also, it can be stated that the proposed PFC approach has proved its effectiveness through achieving the control targets and minimizing the deviation (error) between the predicted rotor flux (α-β) components and their references as can be observed in Figures 64 and 65, respectively.

Moreover, by comparing the number of commutations which has been developed by the two control approaches during the implementation, it can be realized that the proposed PFC exhibits less computational burden than the PTC and this is addressed in Table 4.

A detailed view about the absolute error variation when operating at synchronous speed for the PFC approach can be shown in Figures 73, 74 and 75 which illustrate the absolute error, the cost function values and voltage index, respectively. Comparing with the values obtained under the PTC and shown in Figures 70, 71 and 72, the PFC introduces lower average error of 0.027 compared with an average error of 0.136 for the PTC.

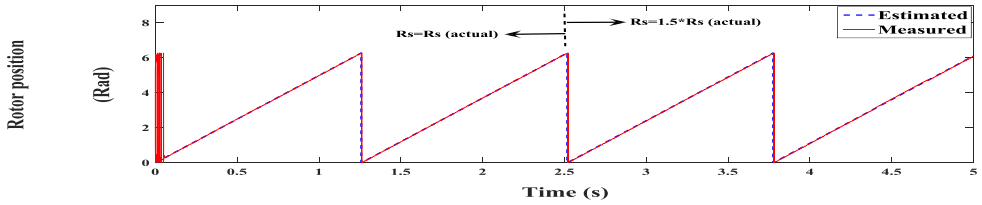

FIGURE 100. Estimated rotor position under PFC at low speed.

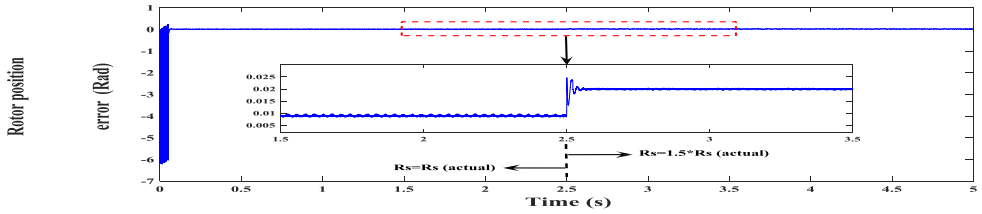

FIGURE 101. Rotor position estimation error under PFC at low speed.

TABLE 5. Stator currents FFT for PTC and proposed PFC at low speed.

	PTC		Proposed PFC	
	Fundamental	THD	Fundamental	THD
Phase 'a'	87.3835 A	15.98 %	87.8121 A	5.42 %
Phase 'b'	88.1829 A	13.72 %	87.7327 A	5.08 %
Phase 'c'	86.4289 A	14.92 %	86.5889 A	6.28 %

C. TESTING AT LOW SPEED

The DFIG performance under the proposed PFC and PTC procedures is also tested at very low speed operation (about 1% of synchronous speed). The superiority of the proposed PFC over the PTC is confirmed again through the obtained results shown in Figures 86, 87, 88, 89, 90, 91 and 92 which represent the torque, rotor flux, active and reactive powers, stator flux, stator and rotor currents, respectively. These figures show a reduced ripples content compared with their corresponding values which are obtained under the PTC and shown through Figures 76, 77, 78, 79, 80, 81 and 82, respectively.

A FFT analysis has been carried out for the stator currents obtained using the two control procedures at low speed operation. From the comparison, it can be realized that the proposed PFC has managed in restricting the accompanied harmonics in a better way than the PTC. A FFT comparison can be shown in Table 5.

The feasibility of the rotor current estimation mechanism is confirmed through Figure 92 which shows a finite matching between the estimated and measured rotor currents. Moreover, the control target of the proposed PFC is achieved through the smooth tracking of rotor flux reference values as shown in Figures 96 and 97.

The capability of the proposed PFC in reducing the harmonic contents in the controlled variables can be also observed graphically through the FFT figures of the stator currents shown though Figures 93, 94 and 95 which exhibit fewer harmonic than the obtained values under the PTC which are shown in Figures 83, 84 and 85.

TABLE 6. Number of commutations at low speed.

	PTC	Proposed PFC
COMMUTATIONS	7317	4108
SWITCHING FREQUENCY	1.22 KHz	685 Hz

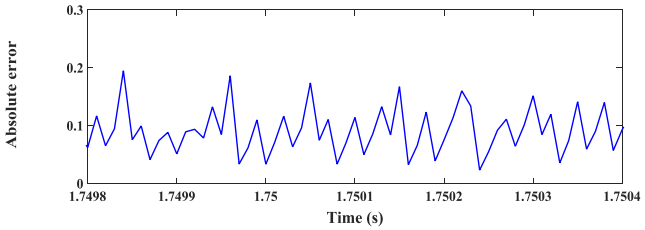

FIGURE 102. Absolute error under PTC at low speed.

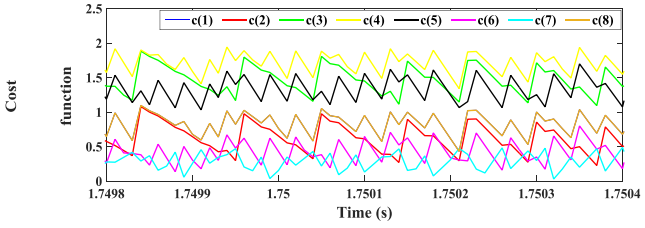

FIGURE 103. Cost function under PTC at low speed.

The robustness of the sensorless rotor position estimator has been verified at low speed operation with a mismatch in the stator resistance of 50%, and this can be confirmed by the obtained result shown in Figures 98 and 99 which illustrate a very good agreement between the estimated and actual unit vectors ($Sin(\theta_{me})$ and $Cos(\theta_{me})$) of the rotor position.

Moreover, the estimated rotor position exhibits a very good agreement with the measured position with minimum error as shown in Figures 100 and 101. At last, the comparison in terms of the commutations number is given in Table 6, which proves the ability of the proposed PFC in reducing the computational time.

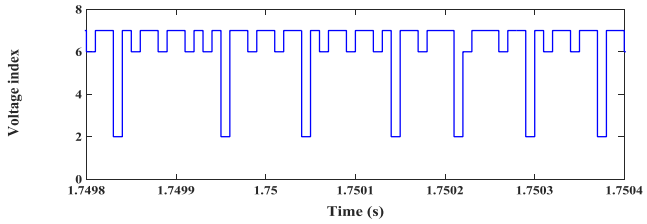

FIGURE 104. Voltage index variation under PTC at low speed.

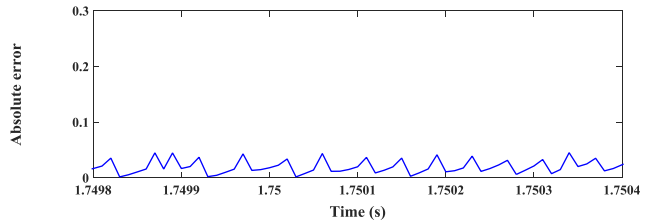

FIGURE 105. Absolute error under PFC at low speed.

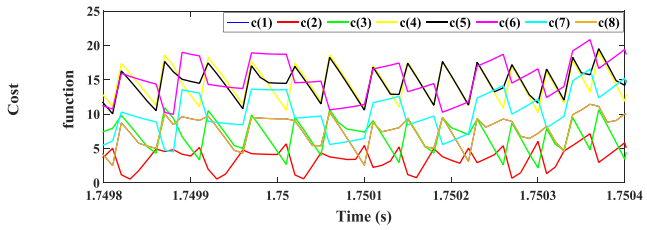

FIGURE 106. Cost function under PFC at low speed.

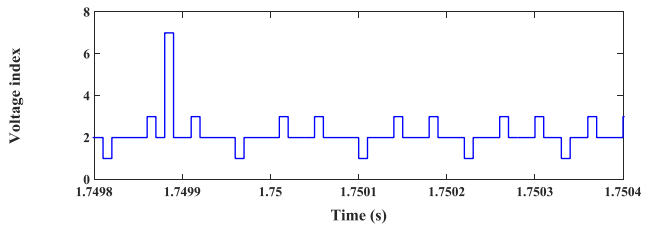

FIGURE 107. Voltage index variation under PFC at low speed.

As an indicator for the ripples content in the controlled variables under the two control procedures, the absolute error value is utilized as a measure. Figures 105, 106 and 107 illustrate the absolute error, the cost function values and voltage index under the PFC approach. While, Figures 101, 103 and 104 show the correspondant values under the PTC. Through comparing both figures, it can be realized that the PFC introduces lower average error of 0.038 compared with an average error of 0.147 for the PTC, which confirm the effectiveness of the proposed PFC in limiting the fluctuations in the controlled variables.

The comparison between the two control procedures (PTC and PFC) can also performed in terms of switching power loss. The amount of energy loss E_{loss} emitted in one transistor per second can be calculated in terms of switching frequency and number of commutations (on and off) by

$$E_{loss} = f_{sw} * \left(E_{on} + E_{off}\right) \tag{62}$$

where f_{sw} is the corresponding switching frequency in Hz, and E_{on}, E_{off} are the energy loss of switching transistor on and off,

TABLE 7. Switching power losses for the three operating cases.

	PTC	Proposed PFC
Transition from sub-synchronous to super-synchronous speed	93.9125 W	29.57526 W
Synchronous speed operation	86.952 W	31.00104 W
Low speed operation	89.2674 W	28.1398 W

TABLE 8. Computation time for the three operating cases.

	PTC	Proposed PFC
Transition from sub-synchronous to super-synchronous speed	18.2 µs	7.3 µs
Synchronous speed operation	16.4 µs	8.1 µs
Low speed operation	17.9 µs	6.7 µs

respectively; measured in Joule and they are function of the number of commutations. The switching power loss can be then calculated from the energy-power relationship defined by

$$E_{loss} = \int_0^t P_{sw,loss} dt \tag{63}$$

The terms of (62) can be obtained with the help of the calculated switching frequencies and number of commutations in addition to the collector-emitter voltage and collector current of the switching transistor. The number of commutations and switching frequencies qre already obtained for the three operating cases of DFIG in the results section. Then, the switching power losses for the three test cases are calculated and addressed in Table 7.

From Table 7, it can be realized that the power switching losses under the proposed PFC are effectively limited comparing with its values under the PTC which confirm the superiority of the proposed PFC approach.

Another analytical comparison between the two control procedures can be performed in terms of the computational time taken during executing the code, and this can be shown through Table 8.

From Table 8, it can be realized that the proposed PFC has effectively managed in reducing the computational time in comparison with the PTC, and this is due to the simplicity of the cost function form of (32).

VIII. CONCLUSION

The paper has presented a robust sensroless predictive flux control (PFC) approach for a doubly fed induction generator. The proposed PFC can be considered as an effective alternative to the predictive power (PPC) and torque control (PTC) approaches with the merits of reduced ripples content and limited total harmonic distortion (THD). Moreover, the proposed PFC exhibits less number of commutations than the PTC which contributes in reducing the computational burden

on the microprocessor. To save the cost, an effective rotor current estimator is used which enables the reduction of the used rotor current sensors. In order to enhance and improve the rotor flux estimation, an effective rotor flux estimator has been proposed, which is then extended to estimate the rotor position. The effectiveness of the sensorless procedure is confirmed through the results which are obtained at different operating speeds (changing from sub-synchronous to super-synchronous speed, at synchronous speed and at very low speed). These results show that the proposed PFC in general has succeeded in achieving the control targets, besides that the estimated rotor position presents high matching degree with the measured position which increases the robustness of the controller through performing precise co-ordinates transformation even under the parameters mismatch. In the future, this work will be extended with experimental implementation to validate the proposed approach with different cases of study such as low voltage grid and unbalanced voltage grid. Moreover, the proposed approach can be also extended to be applied for different types of AC machine drives.

APPENDIX

See Table 9.

TABLE 9. Parameters of DFIG and control system.

Parameters	Value	Parameters	Value
Rated power	55 Kw	L_m	16 mH
R_s	70 mΩ	U_{sn} (nominal stator voltage)	380 v
R_r	87 mΩ	U_{rn} (nominal rotor voltage)	365 v
L_s	16.25 mH	I_{sn} (nominal stator current)	115 A
L_r	16.3 mH	k_p, k_i (PI torque controller)	0.0109 & 0.6861
p (Pole pairs)	3	T_s (Sampling time)	100 µs

REFERENCES

[1] N. Chilakapati, V. S. Ramsden, and V. Ramaswamy, "Performance evaluation of doubly-fed twin stator induction machine drive with voltage and current space vector control schemes," *IEE Proc.-Electr. Power Appl.*, vol. 148, no. 3, pp. 287–292, May 2001.

[2] G. D. Marques and M. F. Iacchetti, "DFIG topologies for DC networks: A review on control and design features," *IEEE Trans. Power Electron.*, vol. 34, no. 2, pp. 1299–1316, Feb. 2019.

[3] N. Dinic, B. Fox, D. Flynn, L. Xu, and A. Kennedy, "Increasing wind farm capacity," *IEE Proc.- Gener., Transmiss. Distrib.*, vol. 153, no. 4, pp. 493–498, Jul. 2006.

[4] R. PeÑa, R. CÁrdenas, J. Proboste, J. Clare, and G. Asher, "Wind–diesel generation using doubly fed induction machines," *IEEE Trans. Energy Convers.*, vol. 23, no. 1, pp. 202–214, Mar. 2008.

[5] D. Zhou, G. Zhang, and F. Blaabjerg, "Optimal selection of power converter in dfig wind turbine with enhanced system-level reliability," *IEEE Trans. Ind. Appl.*, vol. 54, no. 4, pp. 3637–3644, Jul./Aug. 2018.

[6] Y. Han, S. Kim, J.-I. Ha, and W.-J. Lee, "A doubly fed induction generator controlled in single-sided grid connection for wind turbines," *IEEE Trans. Energy Convers.*, vol. 28, no. 2, pp. 413–424, Jun. 2013.

[7] A. Balogun, O. Ojo, and F. Okafor, "Decoupled direct control of natural and power variables of doubly fed induction generator for extended wind speed range using feedback linearization," *IEEE J. Emerg. Sel. Topics Power Electron.*, vol. 1, no. 4, pp. 226–237, Dec. 2013.

[8] X. Wang, H. Lin, and Z. Wang, "Transient control of the reactive current for the line-side converter of the brushless doubly-fed induction generator in stand-alone operation," *IEEE Trans. Power Electron.*, vol. 32, no. 10, pp. 8193–8203, Oct. 2017.

[9] Z. Zheng, C.-J. Huang, R.-H. Yang, X. Xiao, and C. Li, "A low voltage ride through scheme for DFIG-based wind farm with SFCL and RSC control," *IEEE Trans. Appl. Supercond.*, vol. 29, no. 2, Mar. 2019, Art. no. 5601005.

[10] M. Mossa and Y. Mohamed, "Novel scheme for improving the performance of a wind driven doubly fed induction generator during grid fault," *Wind Eng.*, vol. 36, no. 3, pp. 305–334, 2012.

[11] J.-H. Liu, C.-C. Chu, and Y.-Z. Lin, "Applications of nonlinear control for fault ride-through enhancement of doubly fed induction generators," *IEEE J. Emerg. Sel. Topics Power Electron.*, vol. 2, no. 4, pp. 749–763, Dec. 2014.

[12] J. Hu, J. Zhu, and D. G. Dorrell, "A new control method of cascaded brushless doubly fed induction generators using direct power control," *IEEE Trans. Energy Conv.*, vol. 29, no. 3, pp. 771–779, Sep. 2014.

[13] B. Subudhi and P. S. Ogeti, "Optimal preview stator voltage-oriented control of DFIG WECS," *IET Gener., Transmiss. Distrib.*, vol. 12, no. 4, pp. 1004–1013, Feb. 2018.

[14] J. Mohammadi, S. Vaez-Zadeh, S. Afsharnia, and E. Daryabeigi, "A combined vector and direct power control for DFIG-based wind turbines," *IEEE Trans. Sustain. Energy*, vol. 5, no. 3, pp. 767–775, Jul. 2014.

[15] D. Santos-Martin, J. L. Rodriguez-Amenedo, and S. Arnalte, "Direct power control applied to doubly fed induction generator under unbalanced grid voltage conditions," *IEEE Trans. Power Electron.*, vol. 23, no. 5, pp. 2328–2336, Sep. 2008.

[16] J. Hu, H. Nian, B. Hu, Y. He, and Z. Q. Zhu, "Direct active and reactive power regulation of DFIG using sliding-mode control approach," *IEEE Trans. Energy Convers.*, vol. 25, no. 4, pp. 1028–1039, Dec. 2010.

[17] A. Izanlo, S. A. Gholamian, and M. V. Kazemi, "Comparative study between two sensorless methods for direct power control of doubly fed induction generator," *Rev. Roumaine Sci. Techn.-Électrotechn. Et Énerg.*, vol. 62, no. 4, pp. 358–363, Dec. 2017.

[18] A. J. S. Filho, A. L. de Oliveira, L. L. Rodrigues, E. C. M. Costa, and R. V. Jacomini, "A robust finite control set applied to the DFIG power control," *IEEE J. Emerg. Sel. Topics Power. Electron.*, vol. 6, no. 4, pp. 1692–1698, Dec. 2018.

[19] P. Kou, D. Liang, J. Li, L. Gao, and Q. Ze, "Finite-control-set model predictive control for DFIG wind turbines," *IEEE Trans. Autom. Sci. Eng.*, vol. 15, no. 3, pp. 1004–1013, Jul. 2018.

[20] Y. Zhang, D. Xu, and D. Jiang, "A universal multiple-vectors-based model predictive direct power control for doubly fed induction generators," in *Proc. IEEE Energy Convers. Congr. Expo. (ECCE)*, Cincinnati, OH, USA, Oct. 2017, pp. 3337–3344.

[21] M. F. Araya, C. Silva, and P. Cortés, "Predictive current control of a doubly fed inductor generator (DFIG) for fast power reference tracking," in *Proc. 15th Int. Power Electron. Motion Control Conf. (EPE/PEMC)*, Novi Sad, Serbia, Sep. 2012, pp. DS2a.5-1–DS2a.5-6.

[22] G. Iwanski, T. Łuszczyk, P. Pura, and M. Szypulski, "Indirect torque and stator reactive power control of doubly fed induction machine connected to unbalanced power network," *IEEE Trans. Energy Convers.*, vol. 31, no. 3, pp. 1202–1211, Sep. 2016.

[23] J. Hu, J. Zhu, Y. Zhang, G. Platt, Q. Ma, and D. G. Dorrell, "Predictive direct virtual torque and power control of doubly fed induction generators for fast and smooth grid synchronization and flexible power regulation," *IEEE Trans. Power Electron.*, vol. 28, no. 7, pp. 3182–3194, Jul. 2013.

[24] S. Mondal and D. Kastha, "Improved direct torque and reactive power control of a matrix-converter-fed grid-connected doubly fed induction generator," *IEEE Trans. Ind. Electron.*, vol. 62, no. 12, pp. 7590–7598, Dec. 2015.

[25] V. P. Muddineni, A. K. Bonala, and S. R. Sandepudi, "Enhanced weighting factor selection for predictive torque control of induction motor drive based on VIKOR method," *IET Electr. Power Appl.*, vol. 10, no. 9, pp. 877–888, 2016.

[26] V. P. K. Kunisetti, R. E. K. Meesala, and V. K. Thippiripati, "Improvised predictive torque control strategy for an open end winding induction motor drive fed with four-level inversion using normalised weighted sum model," *IET Power Electron.*, vol. 11, no. 5, pp. 808–816, May 2018.

[27] A. Izanlo, S. A. Gholamian, and M. V. Kazemi, "A new method of predictive direct torque control for doubly fed induction generator under unbalanced grid voltage," *Rev. Roumaine Sci. Techn.-Electrotechn. Et Energ.*, vol. 63, no. 3, pp. 332–337, Sep. 2018.

[28] A. Izanlo, S. A. Gholamian, and M. V. Kazemi, "Using of four-switch three-phase converter in the structure DPC of DFIG under unbalanced grid voltage condition," *Elect. Eng.*, vol. 100, no. 3, pp. 1925–1938, 2018.

[29] M. M. Vayeghan and S. A. Davari, "Torque ripple reduction of DFIG by a new and robust predictive torque control method," *IET Renew. Power Gener.*, vol. 11, no. 11, pp. 1345–1352, Sep. 2017.
[30] V. Vimlesh, C. Chandan, M. Suman, and H. Yoichi, "Speed sensorless vector controlled induction motor drive using single current sensor," *IEEE Trans. Energy Convers.*, vol. 28, no. 4, pp. 938–950, Dec. 2013.
[31] T. M. Wolbank and R. Macheiner, "Scheme to reconstruct phase current information of inverter fed AC drives," *Electron. Lett.*, vol. 38, no. 5, pp. 204–205, Feb. 2002.
[32] H. Kim and T. M. Jahns, "Phase current reconstruction for AC motor drives using a DC link single current sensor and measurement voltage vectors," *IEEE Trans. Power Electron.*, vol. 21, no. 5, pp. 1413–1419, Sep. 2006.
[33] W.-C. Lee, T.-K. Lee, and D.-S. Hyun, "Comparison of single-sensor current control in the DC link for three-phase voltage-source PWM converters," *IEEE Trans. Ind. Electron.*, vol. 48, no. 3, pp. 491–505, Jun. 2001.
[34] S. Thomsen, K. Rothenhagen, and F. W. Fuchs, "Online parameter identification methods for doubly fed induction generators," in *Proc. IEEE Power Electron. Spec. Conf.*, Rhodes, Greece, Jun. 2008, pp. 2735–2741.
[35] A. N. Smith, S. M. Gadoue, and J. W. Finch, "Improved rotor flux estimation at low speeds for torque MRAS-based sensorless induction motor drives," *IEEE Trans. Energy Convers.*, vol. 31, no. 1, pp. 270–282, Mar. 2016.
[36] A. Susperregui, J. Jugo, I. Lizarraga, and G. Tapia, "Automated control of doubly fed induction generator integrating sensorless parameter estimation and grid synchronisation," *IET Renew. Power Gener.*, vol. 8, no. 1, pp. 76–89, Jan. 2014.

MAHMOUD A. MOSSA received the bachelor's and master's degrees in electrical engineering from the Faculty of Engineering, Minia University, Egypt in 2008 and 2013, respectively, and the Ph.D. degree in electrical engineering (control of electric machine drives) from the Electric Drives Laboratory (EDLAB), University of Padova, Italy, in April 2018. Since January 2010, he has been an Assistant Lecturer with the Electrical Engineering Department, Minia University. Since May 2018, he has been an Assistant Professor with the Electrical Engineering Department, Minia University. His research interests are focused on electric machine drives, renewable energy systems, and power electronics.

AMEENA SAAD AL-SUMAITI received the B.Sc. degree in electrical engineering from United Arab Emirates University, United Arab Emirates, in 2008, and the M.A.Sc. and Ph.D. degrees in electrical and computer engineering from the University of Waterloo, Canada, in 2010 and 2015, respectively. She was a Visiting Assistant Professor with MIT, Cambridge, MA, USA, in 2017. She is currently an Assistant Professor with the Advanced Power and Energy Center, Department of Electrical Engineering and Computer Science, Khalifa University, Abu Dhabi, United Arab Emirates. Her research interests include power systems, intelligent systems, energy economics, and energy policy.

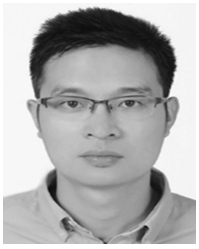

TON DUC DO (S'12–M'14–SM'19) received the B.S. and M.S. degrees in electrical engineering from the Hanoi University of Science and Technology, Hanoi, Vietnam, in 2007 and 2009, respectively, and the Ph.D. degree in electrical engineering from Dongguk University, Seoul, South Korea, in 2014.

From 2008 to 2009, he was a Lecturer with the Division of Electrical Engineering, Thuy Loi University, Vietnam. He was a Postdoctoral Researcher with the Division of Electronics and Electrical Engineering, Dongguk University, in 2014. He was a Senior Researcher at the Pioneer Research Center for Controlling Dementia by Converging Technology, Gyeongsang National University, South Korea, from May 2014 to August 2015. Since September 2015, he has been an Assistant Professor with the Department of Robotics and Mechatronics, Nazarbayev University, Kazakhstan. His research interests include the field of advanced control system theories, electric machine drives, renewable energy conversion systems, uninterruptible power supplies, and electromagnetic systems with nanorobots.

Dr. Do received the Best Research Award from Dongguk University, in 2014. He was the Lead Guest Editor for the Special Issue of Mathematical Problems in Engineering on Advanced Control Methods for Systems With Fast-Varying Disturbances and Applications. He is also an Associate Editor of IEEE Access.

AHMED A. ZAKI DIAB received the B.Eng. and M.Eng. degrees in electrical engineering from Minia University, Egypt, in 2006 and 2009, respectively, and the Ph.D. degree from Novosibirsk State Technical University, Novosibirsk, Russia, in 2015. He was a Postdoctoral Research Fellow with the Moscow Power Engineering Institute, Moscow, Russia, for six months in 2017/2018. He is currently an Assistant Professor with the Electrical Engineering Department, Faculty of Engineering, Minia University. Since July 2019, he has been a Postdoctoral Researcher with the Green Power Electronics Circuits Laboratory, Kyushu University, Japan. His current research interests include renewable energy systems, power electronics, and machines drives.